A Conceptual Model of Polar Overturning Circulations

Thomas W. N. Haine*

Earth & Planetary Sciences, Johns Hopkins University, Baltimore, Maryland

Corresponding author: Thomas W. N. Haine, Thomas.Haine@jhu.edu

ABSTRACT

The global ocean overturning circulation carries warm, salty water to high latitudes, both in the Arctic and Antarctic. Interaction with the atmosphere transforms this inflow into three distinct products: sea ice, surface Polar Water, and deep Overflow Water. The Polar Water and Overflow Water form estuarine and thermal overturning cells, stratified by salinity and temperature, respectively. A conceptual model specifies the characteristics of these water masses and cells given the inflow and air/sea/land fluxes of heat and freshwater. The model includes budgets of mass, salt, and heat, and parametrizations of Polar Water and Overflow Water formation, which include exchange with continental shelves. Model solutions are mainly controlled by a linear combination of air/sea/ice heat and freshwater fluxes and inflow heat flux. The model shows that for the Arctic, the thermal overturning is likely robust, but the estuarine cell appears vulnerable to collapse via a so-called heat crisis that violates the budget equations. The system is pushed towards this crisis by increasing Atlantic Water inflow heat flux, increasing meteoric freshwater flux, and/or decreasing heat loss to the atmosphere. The Antarctic appears close to a so-called Overflow Water emergency with weak constraints on the strengths of the estuarine and thermal cells, uncertain sensitivity to parameters, and possibility of collapse of the thermal cell.

1. Introduction

The global ocean overturning circulation is transformed in the high latitudes of both hemispheres. The transformation is achieved by extraction of heat to the atmosphere, addition of meteoric freshwater, and interaction with ice. Understanding how warm salty inflows to polar oceans partition into different outflow components is primitive, however, and this question is important for oceanography and climate science. To address it, this paper presents and explores a conceptual physical model and applies it to both the Arctic and the Antarctic.

The Arctic Ocean and Nordic Seas are separated from the global ocean by relatively shallow ridges between Greenland and Scotland. The flow across these ridges consists of surface-intensified warm salty water from the North Atlantic Current flowing north (Hansen et al. 2008). Returning south are three distinct water types (Hansen and Østerhus 2000; Østerhus et al. 2005). First, there is overflow water, which spills into the North Atlantic Ocean through gaps in the ridges. Overflow water is cooler and denser than the inflow, but of similar salinity. Second, there is a cold fresh surface outflow in the East Greenland Current (Rudels et al. 2002). The East Greenland Current also carries the third water type, which is sea ice.

The exchange between the Nordic Seas and the Arctic Ocean across the Fram Strait and Barents Sea Opening is essentially the same. Fig. 1 shows the hydrographic characteristics and currents. The warm salty inflow is Atlantic Water (AW), which flows north in the eastern halves of the Barents Sea Opening and the Fram Strait. The net AW flux into the Arctic is about 4 Sv (Tsubouchi et al. 2012, 2018; some also recirculates in Fram Strait; 1 Sv equals $10^6 \mathrm{m}^3\mathrm{s}^{-1}$). The AW temperature exceeds about 3^{o}C with a salinity around 35.00 g/kg and a seasonal cycle that leads to summer surface freshening and warming (Fig. 1 lower panel). The three outflows are Overflow Water (OW), which is cooler and denser than AW, but of similar salinity (the closest water type from

Tsubouchi et al. (2018) is their Intermediate Water, but we adopt OW here, consistent with Eldevik and Nilsen 2013). OW leaves the Arctic on the western side of Fram Strait in the deep part of the East Greenland Current. Above OW is Polar Water (PW), which is near the freezing temperature and fresher than AW (Tsubouchi et al. 2018 call this Surface Water). As for AW, the PW is warmer and fresher in summer. Sea ice occupies the western part of Fram Strait and the East Greenland continental shelf, flowing in the East Greenland Current. The split between OW and PW transport is about 3:1 (this estimate, from Tsubouchi et al. 2018 Fig. 4, is representative not precise, due mainly to the non-zero flow across Fram Strait and the Barents Sea Opening). The sea ice flux is about 0.064 Sv (Haine et al. 2015).

The Antarctic overturning circulation is essentially similar. The inflow of warm salty water occurs in Circumpolar Deep Water (CDW), analogous to AW (it is called AW below), and fed from the North Atlantic overflows. CDW upwells towards the surface beneath the Antarctic Circumpolar Current (Marshall and Speer 2012; Talley 2013). Air/sea/ice interaction around Antarctica transforms the CDW in two meridional overturning cells that circulate back north. The stronger cell is the upper one with a transport of about 22 Sv, equivalent to 80% of the CDW flux (Abernathey et al. 2016; Pellichero et al. 2018). This cell feeds fresh, cold surface water that is called Winter Water when the summer thermal stratification is removed. It is analogous to Arctic PW. The Winter Water flows north and subducts as Subantarctic Mode Water (SAMW) and Antarctic Intermediate Water (AAIW), which are less dense than CDW mainly because they are fresher. Associated with Winter Water is sea ice, which forms primarily near Antarctica in winter and flows north with a flux of about 0.36 Sv (Abernathey et al. 2016). The weaker, lower cell produces Antarctic Bottom Water (AABW) from CDW by cooling and salinification. AABW is analogous to Arctic OW. It forms from CDW by freezing and brine rejection, especially on the continental shelves in the Weddell and Ross Seas and around east Antarctica (Foster and Carmack

1976; Orsi et al. 1999; Jacobs 2004). The resulting dense, saline, freezing shelf water overflows the shelf break into the deep ocean. As it descends, the dense plume entrains and mixes with ambient CDW to form AABW (Muench et al. 2009; Naveira Garabato et al. 2002).

To our knowledge, no prior study quantifies both estuarine and thermal overturning cells in the Arctic and Antarctic. Nevertheless, the key ideas in the present model are well known in the polar oceanography literature. First, consider the salinization process to produce dense shelf water: Gill (1973) argues that brine release during winter freezing on the continental shelves of the Weddell Sea produces dense saline water that overflows the shelf break to form AABW. He points to the wind driven export of sea ice offshore to maintain high freezing rates in coastal polynyas. This process is corroborated using satellite microwave data in the Arctic by Tamura and Ohshima (2011). Aagaard et al. (1981) describe the maintenance of the Arctic halocline by salinization of shelf water in winter by freezing and export of sea ice. Their observations show freezing shelf water with high salinity, in some cases 2–4 g/kg higher than in summer. Extending this work, Aagaard et al. (1985) propose that a major source of Arctic deep water is dense brine-enriched shelf water. Quadfasel et al. (1988) present observational evidence of the shelf overflow and entrainment process occurring in Storfjorden, Svalbard. They observe shelf water with salinities of about 35.5 g/kg (about 0.5 g/kg saltier than the AW in Fram Strait) at the freezing temperature (see also Maus 2003). Rudels and Quadfasel (1991) review the importance of dense shelf water overflow to the maintenance of the deep Arctic Ocean thermohaline structure. They conclude that it must dominate open-ocean deep convection, although this latter process occurs variably in the Greenland Sea. Freezing and brine rejection drive both deep convection and shelf overflows in their view, consistent with Aagaard et al. (1985).

More recently, Rudels (2010, 2012) articulates the problem of understanding Arctic water mass transformation and the Arctic estuarine and thermal overturning cells together (he refers to them as

a "double estuary"). His papers address several issues that underpin the present work: formation of the fresh PW layer, conversion of AW to PW, separation between the estuarine and thermal cells, formation of deep water, and exchange through Fram Strait. Abernathey et al. (2016) and Pellichero et al. (2018) also view the Antarctic system in an holistic way. They focus on the upper estuarine cell and the importance of sea ice in fluxing freshwater from the shelves to freshen SAMW and AAIW. Eldevik and Nilsen (2013) define the problem of quantifying the two Arctic overturning cells (they refer to them as the "Arctic-Atlantic thermohaline circulation"). Their model consists of volume, salinity, and heat budgets, similar to eq. (1) below. However, to close their problem and solve for the outflow transports they must specify the temperature and salinity properties of PW and OW. They also neglect sea ice. Therefore, their system is a special case of the model presented here, which does not make these assumptions.

This paper synthesizes the ideas outlined above. It builds, explains, and applies a quantitative model of polar overturning circulation. The model is conceptual so as to elucidate principles and characteristics. It neglects many important effects including seasonality, interannual variability, regional differences, and continuously varying hydrographic properties. It includes budgets for mass, salt, and heat and physical parametrizations of PW and OW formation. Although it respects physical principles, the model is essentially kinematic. The dynamics of the overturning circulations are beyond the model's scope, and likely differ between the Arctic and Antarctic. Nevertheless, the dynamics must in aggregate respect the budget and parametrization equations used here.

2. Conceptual Model

Consider the system sketched in Fig. 2: A deep polar basin is fed across a gateway from lower latitudes with relatively warm, salty Atlantic Water (AW). The polar basin connects to a shallow

polar continental shelf across a shelf break. The basin and shelf exchange heat and freshwater with the atmosphere. The basin returns three distinct water classes to lower latitudes (see Fig. 3 for a temperature/salinity schematic), namely: Overflow Water (OW), which is a cooled, denser version of AW, with similar salinity; Polar Water (PW), which is a fresh, freezing, less dense version of AW; and, sea ice. Sea ice formation (freezing) occurs on the shelf and there is partial sea ice melting in the basin. The AW to OW pathway comprises the thermal overturning cell and the AW to PW plus sea ice comprises the estuarine overturning cell.

The model specifies steady seawater mass, heat, and salt mass budgets for two control volumes: the basin melting region and the continental shelf freezing region (see also Eldevik and Nilsen 2013). In the **basin** (region A):

$$\begin{aligned}
\rho_1 U_1 + \rho_2 U_2 + \rho_3 U_3 + \rho_i U_i - \rho_1 u_1 - \rho_i u_i - \rho_s u_s &= \mathcal{F}_b, \\
\rho_1 U_1 S_1 + \rho_2 U_2 S_2 + \rho_3 U_3 S_3 + \rho_i U_i S_i - \rho_1 u_1 S_1 - \rho_i u_i S_i - \rho_s u_s S_s &= 0, \\
c_p \left(\rho_1 U_1 T_1 + \rho_2 T_2 U_2 + \rho_3 T_3 U_3 - \rho_1 T_1 u_1 - \rho_s T_s u_s\right) - \rho_i L' \left(U_i - u_i\right) &= \mathcal{Q}_b. \qquad (1)
\end{aligned}$$

Full details on notation are in Table 1. For now, note that state variables are blue, intermediate variables are brown (or green if they satisfy an inequality), flux parameters are red, and **constants** are **black**. The volume fluxes (transports) are U_j, temperatures are T_j, and salinities are S_j (the associated density is $\rho_j = \rho(T_j, S_j)$). The j subscripts correspond to: 1 = Atlantic Water (AW), 2 = Polar Water (PW), 3 = Overflow Water (OW). The AW flux parameters $U_1, U_1 T_1$ and $U_1 S_1$ are provided. The surface ocean freshwater mass and heat flux parameters are $\mathcal{F}_b$[1] and $\mathcal{Q}_b$, respectively. The sign conventions are:

- Positive volume fluxes U_j mean poleward flow. So U_1 is positive and all the others are negative.

[1]Inflowing freshwater is assumed to have a temperature of 0°C.

- Positive fluxes $\mathcal{F}_b$, $\mathcal{Q}_b$ mean ocean to atmosphere freshwater and heat fluxes (i.e., ocean salinifying and cooling). So $\mathcal{F}_b$ is negative and $\mathcal{Q}_b$ is positive.

Assume that not all the sea ice melts, $U_i \leq 0$, and therefore

$$T_2 = T_f, \tag{2}$$

where T_f is the freezing temperature (evaluated at the appropriate salinity, which is S_2 here). Finally, $L' = L - c_p T_f + c_i \left(T_f - T_i\right)$, L is the latent heat of freezing for seawater, T_i is sea ice temperature, and c_p, c_i are the specific heat capacities of seawater and sea ice, respectively.

Similarly, on the **shelf** (region B):

$$\begin{aligned}
\rho_1 u_1 + \rho_s u_s + \rho_i u_i &= \mathcal{F}_s, \\
\rho_1 S_1 u_1 + \rho_s S_s u_s + \rho_i S_i u_i &= 0, \\
c_p \left(\rho_1 T_1 u_1 + \rho_s T_f u_s\right) - \rho_i L' u_i &= \mathcal{Q}_s,
\end{aligned} \tag{3}$$

where the lower case u's indicate the shelf break fluxes and the subscript s indicates Shelf Water (SW) properties. Assume that SW forms from AW by cooling and freshwater input (with no PW contribution). The products are SW with properties T_s, S_s and sea ice that leaves the shelf for the basin. Freezing requires that $u_i \leq 0$ and therefore

$$T_s = T_f. \tag{4}$$

Assume that PW is formed from AW by heat loss to the atmosphere and to melt sea ice, following Klinger and Haine (2019) Chapter 10. See also Rudels (2016), references therein, Abernathey et al. (2016); Pellichero et al. (2018) and Fig. 3. The AW is cooled to freezing temperature and freshened by melt. In order to maintain the stably stratified PW layer above the AW layer, we require that

$\rho_2 \leq \rho_1$. This sets the maximum allowed PW salinity given the AW inflow properties:

$$S_2 \leq \frac{\beta\,(S_1 - S_i)\left(L' + c_p T_f\right) S_1 + \alpha\left(T_1 - T_f\right)\left(L' + c_p T_1\right) S_i}{\beta\,(S_1 - S_i)\left(L' + c_p T_f\right) + \alpha\left(T_1 - T_f\right)\left(L' + c_p T_1\right)}, \tag{5}$$

where α and β are the thermal expansion and haline contraction coefficients (evaluated at the AW temperature and salinity).

Assume that OW is formed from SW and a mixture of AW and PW that is entrained during the overflow. The Price and O'Neil Baringer (1994) model is used for this process (their end-point model, not the streamtube model: see also discussion in section 4). It computes the product properties of the plume of OW descending from a marginal sea and entraining ambient water (aW). Consider two cases:

- Entraining case for $F_{\text{geo}} \geq 1, \Phi > 0$:

$$T_3 = \Phi T_a + (1 - \Phi) T_s,$$

$$S_3 = \Phi S_a + (1 - \Phi) S_s, \tag{6}$$

  where $(T_s = T_f, S_s)$ are the SW properties, (T_a, S_a) are the aW properties (i.e., the water that is entrained), and the entrainment parameter $0 \leq \Phi \leq 1$ is

$$\Phi = 1 - F_{\text{geo}}^{-2/3} \tag{7}$$

  for geostrophic Froude number

$$F_{\text{geo}} = \frac{g\,(\rho_s - \rho_a)\,\alpha_{\max}^{3/2}\left(W_s + 2K_{\text{geo}} x\right)^{1/2}}{\rho_0 f^{3/2} {u_s}^{1/2}}. \tag{8}$$

  The parameters in (8) are: g gravitational acceleration, ρ_0 seawater reference density, $\alpha_{\max}$ maximum bathymetric slope (not thermal expansion coefficient), f Coriolis parameter, K_{geo} the geostrophic Ekman number, x the distance downstream from the shelf break, W_s the initial plume width at the shelf, and u_s the initial plume volume flux leaving the shelf. In deriving

(8), Price and O'Neil Baringer (1994) assume the plume is geostrophic and the bottom stress causes the plume to grow downstream in width.

- Non-entraining case for $F_{\text{geo}} \leq 1, \Phi = 0$ (see also section 4):

$$T_3 = T_s,$$
$$S_3 = S_s. \tag{9}$$

Whether or not entrainment occurs, this overflow model prescribes two more equations to compute the OW properties, (T_3, S_3).

Additional assumptions are:

1. The aW properties (entrained in the plume) are set by a mixture, $0 \leq \phi \leq 1$, between surface PW and AW:

$$T_a = \phi T_f + (1 - \phi)\, T_1,$$
$$S_a = \phi S_2 + (1 - \phi)\, S_1. \tag{10}$$

The mixture fraction ϕ is formally another parameter in the conceptual model. It is constrained, however, and it is initially held fixed. Section 3g discusses this assumption.

2. The volume flux of OW leaving the system equals the flux after entrainment ceases:

$$U_3 = \frac{u_s}{1 - \Phi}. \tag{11}$$

This last equation is another constraint on the system.

a. *Conceptual Model Equations*

The full system is therefore:

$$\begin{aligned}
\rho_1 U_1 + \rho_2 U_2 + \rho_3 U_3 + \rho_i U_i - \rho_1 u_1 - \rho_s u_s - \rho_i u_i &= \mathcal{F}_b, \\
\rho_1 U_1 S_1 + \rho_2 U_2 S_2 + \rho_3 U_3 S_3 + \rho_i U_i S_i - \rho_1 u_1 S_1 - \rho_s u_s S_s - \rho_i u_i S_i &= 0, \\
c_p \left(\rho_1 U_1 T_1 + \rho_2 U_2 T_f + \rho_3 U_3 T_3 - \rho_1 u_1 T_1 - \rho_s u_s T_f \right) - \rho_i L' \left(U_i - u_i \right) &= Q_b, \\
\rho_1 u_1 + \rho_s u_s + \rho_i u_i &= \mathcal{F}_s, \\
\rho_1 u_1 S_1 + \rho_s u_s S_s + \rho_i u_i S_i &= 0, \\
c_p \left(\rho_1 u_1 T_1 + \rho_s u_s T_f \right) - \rho_i L' u_i &= Q_s, \qquad (12)
\end{aligned}$$

with intermediate variables:

$$T_a = \phi T_f + (1 - \phi) T_1, \qquad (13)$$

$$S_a = \phi S_2 + (1 - \phi) S_1, \qquad (14)$$

$$\rho_a = \rho (T_a, S_a), \qquad (15)$$

$$\rho_2 = \rho \left(T_f, S_2 \right)$$

$$\rho_s = \rho \left(T_f, S_s \right) \qquad (16)$$

$$\Phi = 1 - \gamma \frac{|u_s|^{1/3}}{(\rho_s - \rho_a)^{2/3}}, \qquad (17)$$

$$T_3 = \Phi T_a + (1 - \Phi) T_f, \qquad (18)$$

$$S_3 = \Phi S_a + (1 - \Phi) S_s, \qquad (19)$$

$$\rho_3 = \rho (T_3, S_3), \qquad (20)$$

$$u_s = (1 - \Phi) U_3, \qquad (21)$$

$\gamma = \rho_0^{2/3} f g^{-2/3} \alpha_{\max}^{-1} \left(W_s + 2K_{\text{geo}} x\right)^{-1/3}$ (see section 3j), and $L' = L - c_p T_f + c_i \left(T_f - T_i\right)$. The inequalities are:

$$S_2 \leq \frac{\beta \left(S_1 - S_i\right) \left(L' + c_p T_f\right) S_1 + \alpha \left(T_1 - T_f\right) \left(L' + c_p T_1\right) S_i}{\beta \left(S_1 - S_i\right) \left(L' + c_p T_f\right) + \alpha \left(T_1 - T_f\right) \left(L' + c_p T_1\right)}, \tag{22}$$

$$u_i < U_i < 0, \tag{23}$$

$$U_2, U_3, u_s < 0, \tag{24}$$

$$u_1 > 0, \tag{25}$$

$$\rho\left(T_f, S_s\right) \geq \rho\left(T_3, S_3\right) \geq \rho\left(T_1, S_1\right), \tag{26}$$

$$0 \leq \{\Phi, \phi\} \leq 1. \tag{27}$$

This is a system of six equations in six unknowns, namely, $\{U_2, U_3, U_i, u_1, u_i, S_s\}$, with intermediate variables $\{\rho_2, \rho_3, \rho_s, \rho_a, T_3, T_a, S_3, S_a, u_s, \Phi\}$. There are five flux parameters: $\{U_1, U_1 T_1, U_1 S_1, \mathcal{Q} = \mathcal{Q}_b + \mathcal{Q}_s, \mathcal{F} = \mathcal{F}_b + \mathcal{F}_s\}$, with intermediate parameter $\rho_1 = \rho\left(T_1, S_1\right)$, and the overflow mixing fraction ϕ.

b. Numerical Solution

The model consists of coupled nonlinear algebraic equations. The most important nonlinearity is due to the parametrization of entrainment (17) and (21), although there are several others due to the advective product of variables, like $T_3 U_3$, and seawater functions of state, like $\rho_3 = \rho(T_3, S_3)$. Therefore, the system is solved numerically using a procedure explained in supplement section S1. Numerical solutions satisfy the equations exactly except for (17), which is satisfied within a tolerance $\delta\Phi$ because this is likely the most uncertain part of the model. For a given parameter set, there are typically zero or an infinite number of solutions. The infinite number of solutions is bounded within limits, which are typically tight.

3. Results

a. Arctic Reference Solutions and Sensitivity to Q

Fig. 4 shows results from experiment 1 using parameters roughly appropriate to the Fram Strait and Barents Sea Opening. The parameters (Table 2) are $U_1 = 4.75$ Sv, $T_1 = 3.4^{\circ}$C, $S_1 = 35.00$ g/kg, $Q = 115$ TW, and $\mathcal{F} = -180 \times 10^6$ kgs^{-1}, which are taken from Tsubouchi et al. (2012) and Tsubouchi et al. (2018). The temperature/salinity diagram in Fig. 4 shows the properties of the various water masses. The OW properties T_3, S_3 range over different values, which correspond to a range of SW salinities S_s. Notice that the OW and PW properties are moderately realistic compared to the data shown in Fig. 1. The SW salinities are high, however, and the OW properties cluster close to the aW (indicated by the blue cross). This fact indicates that the entrainment is high for this solution, and indeed, $\Phi = 0.94$. Therefore, the shelf circulation is relatively weak and most OW is formed by AW being entrained into the overflowing SW. Hence, the OW temperature T_3 is relatively high. In this experiment the system balances the heat budget by exporting warm OW. Indeed, experiment 1 has a strong thermal overturning cell compared to the estuarine cell, $U_3/U_2 \approx 3.4$. This ratio is moderately realistic compared to the data shown in Fig. 1 (section 1). The ice export flux, $|U_i|/U_1 \approx 0.040$, is also moderately realistic.

Notice the blue error bars in Fig. 4. They indicate the full range of possible solutions for the fixed parameters in experiment 1 (namely, the 0 and 100 percentiles). The bars themselves indicate the solution with entrainment closest to the mean entrainment (other choices are possible). There are two reasons that a range of solutions exists (see supplement section S1). First, for the fluxes in and out of the system as a whole (across section A; left column in Fig. 4), multiple solutions exist for $\{U_2, U_3, U_i, S_s\}$, and hence $\{u_s, T_3, S_3, \Phi\}$. This multiplicity reflects a tradeoff between shelf salinity S_s and entrainment Φ and is discussed below in section 3c. Second, for the fluxes across the shelf

break (across section B; right column in Fig. 4), multiple solutions exist for u_1 and u_i (in principle, for every value of S_s; the bars show the mean values). This multiplicity reflects a tradeoff between the ocean surface fluxes Q_s and $\mathcal{F}_s$ on the shelf (it is a linear relation, see (S5)). Physically, this second tradeoff means that the shelf heat budget can be satisfied with relatively large Q_s (which is positive), large u_i, large $\mathcal{F}_s$ (negative), and small u_s; or vice versa. The system can lose more or less heat over the shelf relative to the basin, and thereby form more or less sea ice, without disturbing the balance across section A.

Next consider Fig. 5, which shows results from experiment 2. This experiment is the same as experiment 1, except that the total ocean heat loss Q is one third higher (Table 2). The mass fluxes across section A, U_2 and U_3, are similar, $U_3/U_2 \approx 3.8$. The ice export flux for experiment 2 is also similar, $|U_i|/U_1 \approx 0.036$, to experiment 1. Nevertheless, the solution is qualitatively different because it shows strong shelf circulation, cold OW, and weak entrainment ($\Phi = 0.13$). In this experiment, to satisfy the heat budget across section A, the OW is cold. That is achieved by the AW flowing onto the shelf, where it is cooled to freezing, and then flowing off the shelf to form OW with little entrainment. The system cannot satisfy the heat budget with a weak shelf circulation, warm OW, and strong entrainment, like in experiment 1. By switching to this other mode of solution (strong shelf circulation), the system accommodates the greater ocean heat loss.

Now consider Fig. 6, which shows results from experiment 3. This experiment extends experiments 1 and 2 to cover a wide range of Q values (Table 2). Fig. 6 shows the key solution variables as functions of Q. In each panel, the thick lines show the solution with entrainment closest to the mean entrainment (like the bars in Figs. 4 and 5). The coloured patches show the range of possible solutions (like the error bars in Figs. 4 and 5). Experiments 1 and 2 are shown with solid and dashed lines, respectively. Notice first that the entrainment Φ (bottom panel of Fig. 6) reflects the shelf circulation switching on (small Φ) and off (large Φ) according to Q. Large Q

demands strong shelf circulation to supply a large heat flux from the AW to SW to OW conversion process. Second, notice that the range of possible solutions is relatively small for experiments 1 and 2, but between them, at $Q/(\rho_i L' U_1) \approx 0.09$, it is large. In this case, the relative strengths of the shelf circulation and of the PW/OW mass flux ratio are essentially unconstrained (see section 3d). Finally, notice that the range of possible solutions shrinks to zero for small and large Q (to the left and right of experiments 1 and 2 in Fig. 6, respectively). At these limits U_2 approaches zero and for $Q/(\rho_i L' U_1) \lessapprox 0.07$ or $Q/(\rho_i L' U_1) \gtrapprox 0.11$, no negative U_2 solutions are possible. The system no longer makes PW–the hatched regions in Fig. 6–and the estuarine circulation collapses.

b. Collapse of the Estuarine Overturning Cell: Heat and Salt Crises

Collapse of the estuarine circulation can occur for two reasons. For small Q, similar to experiment 1, the shelf circulation is switched off, entrainment is high, and the OW is warm. This state allows maximum export of heat with large OW heat export $-U_3 T_3$ to compensate for the weak ocean heat loss Q. Export of PW or sea ice effectively carries away negative heat, or equivalently imports positive heat to the system (because PW is at the freezing temperature and sea ice is deficient in heat; recall the heat budget is constructed relative to 0°C). Hence, the only way to increase heat export is to increase $-U_3 T_3$. An upper limit to OW temperature T_3 exists, however, which is set by aW temperature T_a (supplement sections S4 and S5). Near this limit (large Φ) the system must compensate for decreased Q by increased OW export $-U_3$. This compensation can only continue as long as the OW mass flux does not exceed the AW mass flux, $-U_3/U_1 \lessapprox 1$, otherwise the PW flux vanishes. This failure mode (meaning loss of viable solutions) is referred to as *heat crisis* because the system can no longer export enough heat and also maintain the estuarine circulation.

The second reason for collapse of estuarine circulation concerns large Q, similar to experiment 2. In this case, the shelf circulation is switched on, entrainment is low, and OW is near the freezing

temperature. This state restricts the export of heat in the thermal cell to supply the large surface heat loss $Q \approx Q_s$. Restricting the export of heat might instead be accomplished by large U_2 and small U_3 (because their temperatures are both freezing). But OW is saltier than PW $S_3 > S_2$, so large U_3 and small U_2 is more efficient at exporting salt. In this state ($U_3 \gg U_2$), greater ocean heat loss Q can be accommodated by more freezing u_i. More freezing necessarily reduces u_s and hence U_3, however, which chokes the export of salt (because sea ice carries very little salt $S_i \ll S_3$). In trying to meet these competing constraints as Q increases, the system is pushed to vanishing U_2 and collapse of the estuarine circulation. This failure mode is referred to as *salt crisis* because the system can no longer export enough salt and also maintain the estuarine circulation.

c. Tradeoff between Entrainment and Shelf Circulation

In Figs. 4 and 5 (experiments 1 and 2) we see solutions with similar thermal and estuarine circulations. In both of them, the OW flux dominates the PW flux by a factor of $U_3/U_2 \approx 3.5$, which is moderately realistic. The shelf circulation strength u_s differs by a factor of about 14 between the experiments, however. Understanding how experiments 1 and 2 maintain the same OW/PW ratio despite the large shelf circulation difference illuminates the model.

Figure 7 shows entrainment Φ against shelf salinity S_s for experiments 1 and 2 (dots). The solid curve comes from a theoretical argument about the tradeoff between these two variables (see supplement section S2). For constant U_3,

$$\Phi = 1 - \frac{\gamma^{3/2}}{\rho_0 \beta \Delta S_s} |U_3|^{1/2}, \tag{28}$$

which says that the shelf salinity anomaly ΔS_s and (one minus the) entrainment are inversely proportional to each other. This gives a good fit to the tradeoff between Φ and S_s at fixed U_3 (see Fig. 7). Physically, it reflects the fact that the AW to OW conversion pathway can either occur by

strong entrainment and weak shelf circulation (experiment 1) or vice versa (experiment 2). AW can either flow directly into OW through entrainment or it can circulate on the shelf before becoming OW. As experiments 1 and 2 show, this tradeoff is important for the heat budget, however. Small (large) Q requires export of warm (cold) OW and therefore a weak (strong) shelf circulation.

d. Unconstrained OW/PW Fluxes: OW Emergency

A variation of this idea explains the wide range of possible solutions for intermediate Q, between experiments 1 and 2 in Fig. 6 (see also supplement section S5). For $Q/(\rho_i L' U_1) \approx 0.09$, the ratio of OW/PW fluxes U_3/U_2 is essentially unconstrained. In this case, the system supports solutions with strong OW flux and weak PW flux that have weak entrainment, strong shelf circulation and cold OW. These solutions are far from the solid curves in Fig. 6, although still within the coloured patches (to balance mass, U_2 must be anti-correlated with U_3 at fixed Q, as seen from the solid lines). This shelf-dominated mode efficiently supplies AW heat to the shelf and hence to the atmosphere via Q_s, like experiment 2. But the system also supports solutions with weak OW flux and strong PW flux (unlike experiments 1 and 2). This intermediate-Q mode balances the heat budget by converting AW mainly to PW (which is cold) and suppressing the export of warm OW. It can have either strong or weak entrainment and shelf circulation: the difference between them is unimportant because little AW is converted to OW in the intermediate mode. This type of solution allows vanishing of the OW thermal overturning cell, $U_3 = 0$, as the solid curve shows for $Q/(\rho_i L' U_1) \approx 0.09$. It is called an *OW emergency*: the thermal cell can disappear, but it does not have to disappear (in contrast, recall that the heat and salt crises require collapse of the estuarine cell). See ahead to section 3j and Fig. 11 for an example of an intermediate-Q solution and OW emergency.

e. Sensitivity to Other System Parameters

Experiments 1, 2, and 3 differ only in $\mathcal{Q}$, the ocean heat loss flux. What about sensitivity to other system parameters? Experiment 4 (Table 2) systematically varies $\{\mathcal{Q}, \mathcal{F}, U_1, T_1, S_1\}$ in 1769472 different combinations ($\phi = 0.33$ is held constant: section 3g explores this parameter). Experiment 4 spans the space of parameters for the Fram Strait and Barents Sea Opening, arising from uncertainty or secular variability. Fig. 8 shows the results for the export volume fluxes. The figure shows histograms of the volume fluxes plotted against

$$\mathcal{N}^* \equiv (1 - S_i/S_1)\,\mathcal{Q} + L'\mathcal{F} + \rho_1 c_p\,(S_i/S_1 - 1)\,T_1 U_1, \tag{29}$$

$$\approx \mathcal{Q} + L\mathcal{F} - \rho_0 c_p U_1 T_1, \tag{30}$$

$$\approx \rho_i L' U_1\,(1 + U_2/U_1 + U_3/U_1)\,. \tag{31}$$

This compound forcing parameter is a function of (mainly) $\mathcal{Q}, \mathcal{F}$, and $U_1 T_1$. It collapses the five dimensional $\{\mathcal{Q}, \mathcal{F}, U_1, T_1, S_1\}$ parameter space onto a line. Distance along this line, $\mathcal{N}^*$, is proportional to $\mathcal{Q}$, but it also depends on the other parameters. In this way, $\mathcal{N}^*$ in experiment 4 and Fig. 8 generalizes $\mathcal{Q}$ in experiment 3 and Fig. 6. The histograms are constructed from the mean entrainment solutions, like the bars in Fig. 4, and the results from experiment 3 are shown with white curves on Fig. 8 for reference. Most of the variation in U_2 among the solutions is controlled by $\mathcal{N}^*$, indicating that this parameter dominates these variations. Equivalently, for a fixed $\mathcal{N}^*$ value, the distribution of U_2 values is relatively tight, especially for $U_2 \to 0$ approaching the heat and salt crises. For example, the range of U_2 values for fixed $\mathcal{N}^*$ is typically smaller than the range of U_2 values about the mean entrainment solution seen in Fig. 4. This is a useful result, because the understanding of the system gained from experiment 3 varying $\mathcal{Q}$ alone, carries over to the full system with varying $\mathcal{Q}, \mathcal{F}, U_1, T_1$ and S_1. Similar remarks apply to the distribution of U_3.

Physically, $\mathcal{N}^*/(\rho_i L' U_1)$ is the fractional anomaly in the volume budget $U_1 + U_2 + U_3 \approx \mathcal{N}^*/(\rho_i L)$, meaning that $\mathcal{N}^*$ measures the (small) difference between the AW transport and the OW and PW transports. Supplement section S3 supports these claims with theoretical arguments, but the main evidence is that the results of experiment 4 in Fig. 8 plotted against $\mathcal{N}^*$ resemble those from experiment 3 in Fig. 6 plotted against $\mathcal{Q}$. In particular, the types of solution and failure mode are the same in experiments 3 and 4.

f. Theory for Parametric Locations of Salt Crisis and OW Emergency

The solution structure in experiments 3 and 4 is determined by the PW crises and the OW emergency. It is useful to understand and quantify the locations in parameter space that define these limiting solutions. Specifically, what is the origin of the salt crisis and OW emergency $\mathcal{Q}/(\rho_i L' U_1) \approx 0.11$ and 0.09 values, respectively, seen in Fig. 6 for experiment 3, or of the limiting values of $\mathcal{N}^*/(\rho_i L' U_1)$ for which $U_2 = 0$, seen in Fig. 8 for experiment 4?

Neither the salt crisis nor the OW emergency involve entrainment. For the salt crisis (like experiment 2), the OW flux is high, the shelf circulation is strong, and entrainment is weak. For the OW emergency, the OW flux collapses, so entrainment is irrelevant because all the inflowing AW converts to PW and flows back out. Therefore, the parametric locations of salt crises and OW emergencies are given by simple functions of the forcing parameters, that can be computed without solving the model. They avoid non-trivial solution of the entrainment model. Supplement section S4 shows details, specifically see (S18) and (S19) for the $\mathcal{Q}$ values that define the two limiting solutions. The results of these formulae are plotted in Fig. 9 against the results from experiment 4 for several hundred solutions very close to salt crisis or OW emergency. The theoretical predictions agree very well with the numerical results.

g. Theory for Parametric Locations of Heat Crisis

What about the heat crises, like the origin of $Q/(\rho_i L' U_1) \approx 0.07$ in Fig. 6, near experiment 1? A non-trivial solution of the entrainment model and the OW properties are now needed. That makes theoretical prediction of the heat crises harder than for salt crises and OW emergencies.

Fig. 9 shows three options, depending on different assumptions (supplement section S4 explains the technicalities). The option with least restrictive assumptions is shown with the green patch. It just requires that the system consistently produces OW with a density greater than or equal to the AW density (so that OW flows out of the system beneath AW). The bounds are robust but relatively wide (Fig. 9). The next option requires knowledge of the aW properties (and hence ϕ), but not the shelf salinity. It gives a moderately accurate estimate of the location of the heat crisis for experiment 4, although it is biased low (green circles in Fig. 9). The option with most restrictive assumptions requires knowledge of both the aW properties (ϕ) and the maximum allowed shelf salinity ${S_s}^{\max}$ (which equals 40 g/kg in all experiments: see section 4). For experiment 4, this option gives an accurate estimate of the parametric location of the heat crisis (green dots in Fig. 9).

The mixing fraction ϕ, and especially, the maximum allowed shelf salinity ${S_s}^{\max}$, are the weakest parts of the model because they are the most uncertain and ad hoc. The processes that determine ϕ and ${S_s}^{\max}$ are beyond the scope of this simple model. Therefore, the theoretical constraints possible on the location of heat crises with various assumptions are reported. Nevertheless, even the option with no assumptions about ϕ and ${S_s}^{\max}$ (green patch in Fig. 9) is useful because it restricts the $\mathcal{N}^*$ parametric location of heat crises. It also quantifies the dependence of the heat crisis on the different forcing parameters (see formula (S20)). This information informs future work on more realistic models that specify ϕ and ${S_s}^{\max}$. For further discussion see section 4.

h. Sensitivity to PW salinity S_2 and Mixing Fraction ϕ: Entrainment Emergency

Recall, that the AW to PW conversion model (section 2) sets an upper limit for the PW salinity. In all experiments shown so far, the PW salinity S_2 equals this limit from (22). This assumption is now relaxed, as is the related assumption that aW has a fixed mixing fraction ϕ.

Figure 10 shows results for experiment 5, which varies S_2 with all other parameters fixed as for experiment 1 (Table 2). There exists a range of possible solutions at moderate entrainment values. As S_2 decreases, the estuarine cell strength U_2 weakens as for the salt and heat crises. For a certain $S_2 \approx 33.5$ g/kg, U_2 vanishes and the estuarine cell disappears. This crisis differs from the salt and heat crises, however, because entrainment $\Phi \approx 0.63$. It is called an *entrainment emergency*. Approaching the entrainment emergency, the aW salinity S_a decreases because the PW salinity S_2 is decreasing. The OW salinity S_3 therefore also decreases. The OW salinity can only decrease until the OW density ρ_3 equals the AW density ρ_1, however, otherwise the stable stratification of AW above OW fails. Therefore, a crisis occurs beyond which entrainment of aW into overflowing shelf water to form OW is no longer possible. The aW becomes too light (fresh) for solutions to the entrainment model to exist. This entrainment emergency also occurs for large ϕ values that make the aW too fresh, for the same reason (see supplement Fig. S1d).

i. Theory for Parametric Location of Entrainment Emergency

The entrainment emergency is understood by noticing that a maximum OW salinity exists, ${S_3}^{\max}$ (see supplement section S6):

$$ {S_3}^{\max} \approx S_a + \frac{\gamma^{3/2}|U_1|^{1/2}}{\rho_0 \beta}. \tag{32} $$

This value minimizes entrainment Φ with a strong thermal overturning cell, $U_3 \approx -U_1$, and a small aW/OW density difference. Similarly, a minimum OW temperature exists, ${T_3}^{\min}$:

$$ {T_3}^{\min} = T_a - \left(T_a - T_f\right) \frac{\gamma^{3/2} |U_1|^{1/2}}{\rho_1 - \rho_a}. \tag{33} $$

In practice, ${S_3}^{\max}$ is a more stringent restriction than ${T_3}^{\min}$ (see the green patches in Figs. 4 and 5). As the aW gets fresher and/or warmer (therefore less dense), these restrictions get tighter. Eventually, the maximum OW salinity equals the minimum allowed OW salinity to keep OW denser than AW. At that point the entrainment emergency is reached.

The aW properties controlling these restrictions depend on ϕ and S_2. In experiment 5, S_2 is decreased until the entrainment emergency occurs for $S_2 \approx 33.5$ g/kg. The corresponding aW temperature and salinity are $T_a = 1.68^{\circ}$C and $S_a = 34.5$ g/kg. From (32), ${S_3}^{\max} \approx 34.78$ g/kg, very close to the value from the numerical solution of $S_3 = 34.70$ g/kg, as seen in Fig. 10. The corresponding OW temperature is $T_3 = 0.35^{\circ}$C (so that $\rho_3 = \rho_1$) and the entrainment fraction is $\Phi = (T_3 - T_f)/(T_a - T_f) \approx 0.63$ from (18), as seen in Fig. 10.

j. Antarctic Reference Solution and Choice of γ

Figure 11 shows a canonical Antarctic solution (experiment 6). The parameters (Table 2) are $U_1 = 26$ Sv (Abernathey et al. 2016), $T_1 = 0.5^{\circ}$C, $S_1 = 34.84$ g/kg (Price and O'Neil Baringer 1994), $\mathcal{Q} = 300$ TW (Volkov et al. 2010), and $\mathcal{F} = -240 \times 10^6$ kgs^{-1} (Abernathey et al. 2016). As for the Arctic solutions, these are representative values with substantial variability and uncertainty. They represent (crudely) the meridional overturning circulation at all longitudes, consistent with the paradigm of zonal-average overturning in the Southern Ocean (Talley 2013; Abernathey et al. 2016; Pellichero et al. 2018). The solution in Fig. 11 has a wide range of OW water properties, entrainment values, and shelf salinities. The canonical solution has $U_2 \approx -16$ Sv, $U_3 \approx -10$ Sv,

and $u_i \approx -0.27$ Sv, which are moderately realistic values (Abernathey et al. 2016; Pellichero et al. 2018). The PW flux nearly always exceeds the OW flux and the system is close to OW emergency. In this sense, the system is more loosely constrained than experiments 1 and 2 and further from heat and salt crises. It is close to switching between strong and weak shelf circulation (Fig. 6).

The Antarctic reference solution reveals an important issue, namely, the choice of entrainment parameter γ from (17). Recall from section 2a that γ sets the sensitivity of entrainment to changes in overflowing SW flux and density difference:

$$\gamma = \frac{\rho_0^{2/3} f}{g^{2/3} \alpha_{\max} \left(W_s + 2K_{\text{geo}} x \right)^{1/3}}. \tag{34}$$

For the Arctic experiments 1–5, $\gamma = 2.2 \times 10^{-3}$ kg$^{2/3}$s$^{1/3}$m^{-3}, which derives from Price and O'Neil Baringer (1994) (their Table 1). The main γ uncertainty is in $W_s + 2K_{\text{geo}}x$, where W_s is the overflow plume width, K_{geo} is the geostrophic Ekman number, and x is downstream distance. This sum is dominated by the plume width W_s for the cases shown here, so focus on W_s. How should W_s vary with the inflow flux U_1, which sets the circulation scale for the problem? The simplest choice, adopted here, is to make W_s proportional to U_1. Physically, that means the shelf system can accommodate arbitrarily broad overflow plumes (technically, it means the problem is linear in U_1). This choice cannot be true for all possible U_1 fluxes of course because of the limits on the length of the shelf break (and the $2K_{\text{geo}}x$ term). But for experiments 1 and 6, W_s = 100 and 550km, respectively, which are short compared to the lengths of the Siberian and Antarctic shelves so the choice appears plausible. In any case, γ has little effect on salt crises because entrainment vanishes for them, or on the possibility of OW emergencies.

4. Discussion

Fig. 12 shows a schematic of the main solution modes for this model, summarizing section 3. The quantitative details of the experiments depend on specific parameter choices, but the qualitative solution modes do not. These modes are organized by PW collapse (loss of the estuarine cell) in heat and salt crises; by unconstrained tradeoff between PW and OW in OW emergency (possible loss of the overturning cell); and by entrainment emergency (loss of the estuarine cell). The transition between these modes is mainly controlled by the compound forcing parameter $\mathcal{N}^*$ (section 3e, eqs. (29)–(31)), which generalizes the effect of the ocean heat loss rate $\mathcal{Q}$. The $\mathcal{N}^*$ parameter estimates the departure from the closed volume budget between AW, OW, and PW. For example, heat crises relate to relatively small OW plus PW transport, indicating relatively large sea ice export. But that occurs for small $\mathcal{N}^*$ (Figs. 4, 6, 9), which is associated with little freezing because the ocean heat loss rate $\mathcal{Q}$ is small. Therefore, a contradiction arises, which is the heat crisis. Similarly, salt crises relate to relatively large OW plus PW transport, indicating small sea ice export, but they occur for large $\mathcal{Q}$. For intermediate $\mathcal{N}^*$ values (near zero), the ratio of OW to PW is loosely constrained because the system can switch between strong and weak shelf circulation strengths (with concomitant weak and strong entrainment). Indeed, the thermal cell can disappear in an OW emergency because the constraints are so loose.

The entrainment emergency is different because it does not mainly depend on $\mathcal{N}^*$. Entrainment emergencies relate to entrained aW becoming too fresh (not dense enough), such as when PW is too fresh. Our approach is to prescribe the aW and PW properties without specifying the physical formation process. The assumption is that the system can freely select aW properties. Therefore, the system can avoid entrainment emergencies by suitable aW and PW choices. In other words, the entrainment emergency does not constrain the possible solution modes for this model, but it

does constrain possible aW and PW properties. These constraints are potentially useful because they can be tight, for example on the minimum allowed PW salinity (Fig. 10).

The sign of the solution sensitivity to forcing parameters depends on the solution location with respect to the crises and emergencies. For example, the estuarine PW cell strengthens as Q increases if entrainment dominates and OW is warm (like experiment 1 in Fig. 6). But the estuarine cell weakens as Q increases if shelf circulation dominates and OW is cold (like experiment 2). The sensitivity of the sea ice export flux to Q also changes sign like this (Figs. 6 and 8). OW thermohaline properties are insensitive to forcing parameters, except when the system switches between strong and weak shelf circulation near the OW emergency. Then, the OW temperature (but not salinity) is very sensitive to forcing changes, which leads to a bimodal distribution of OW temperature (Fig. 6). The OW properties are buffered to changes in shelf salinity in this way. The corollary is that the shelf salinity is relatively unconstrained by the OW properties reflecting the tradeoff between entrainment and shelf circulation (Fig. 7).

The $\mathcal{N}^*$ forcing parameter shows that solution sensitivity depends (essentially) on the individual forcing parameters in a straightforward way (eq. (29)). Specifically, Q changes and freshwater flux changes are interchangeable: greater ocean heat loss compensates greater ocean freshwater gain, and vice versa. Similarly, only the difference between Q and AW heat flux matters, not the individual magnitudes, and the AW salt flux is unimportant. These results emerge from the mass, salt, and heat budgets so they are robust.

The main approximation in this model is the Price and O'Neil Baringer (1994) entrainment parametrization. In particular, uncertainty surrounds the functional form (17), the entrainment sensitivity parameter γ, the maximum shelf salinity ${S_s}^{\max}$, and the aW properties (from PW salinity S_2 and mixing fraction ϕ). Still, the entrainment model is based on firm physical principles. Price and O'Neil Baringer (1994) couple entrainment to the dynamics of the overflow plume, which is

the key ingredient in the present model. Their parametrization says that the dense SW overflowing the shelf break is geostrophic, spreads due to Ekman drainage at the sea floor, and mixes with aW in hydraulic jumps. It makes sense that increasing entrainment depends on increasing SW/aW density difference in (17) because the geostrophic current is proportional to the density difference. It is less obvious that increasing entrainment depends on decreasing SW transport (albeit weakly). The reason is that a larger transport means a thicker overflow plume and therefore a smaller Froude number (because the wave speed increases with plume thickness) and less entrainment. Price and O'Neil Baringer (1994) are guided by the laboratory experiments of Ellison and Turner (1959) and Turner (1986). These studies suggest that mixing during entrainment events is so efficient that the Froude number cannot exceed one. The assumption of geostrophic flow, and thus a geostrophic Froude number in (8), implies the two-thirds exponent in the Froude number scaling (7) (J. Price, pers. comm.). A different exponent would change the details of the switch between strong and weak shelf circulation magnitudes, but not the existence of the switching. Other studies on overflow entrainment point to the importance of entrainment for subcritical flows (Froude number <1, Cenedese and Adduce 2010), especially over rough bottoms (Ottolenghi et al. 2017). Boosting of entrainment by tidal currents is also thought to be important in some situations, such as for AABW in the Ross Sea (Padman et al. 2009). These additional effects are worth exploring, but appear unlikely to make a qualitative difference. The reason is that few solutions have subcritical flow and vanishing entrainment (Figs. 6, 8). On these grounds, the main solution modes in Figs. 6 and 12 probably just require that entrainment grows sensitively with Froude number.

Consider now the maximum SW salinity $S_s^{\max}$ (see section 3g and supplement section S1). This parameter is unavoidable in the numerical method because the entrainment parametrization (17) involves a power law of the aW/SW density (hence salinity) difference. Therefore, no characteristic maximum shelf salinity exists. The upper limit on SW salinity is controlled in reality by other

processes. Most important is exchange across the shelf break jet unrelated to dense overflows, like baroclinic instability (Lambert et al. 2018; Stewart et al. 2018). This exchange augments dense overflows in exporting salt from the shelf (and importing heat on to the shelf). The relative importance of these shelf break exchange mechanisms and their interaction are unclear and worth exploring. The key question is how they control (in order of priority) the OW temperature, OW salinity, and PW salinity because once these variables are known, the budget equations (S1) specify the transports. Despite the uncertainty in what sets $S_s^{\max}$, the results from experiment 5 with a wide range of forcing parameters show that the value chosen here is unimportant: The mean, median, and modal excess SW salinities over AW salinities are just 0.67, 0.04, and -0.06 g/kg, respectively. These are reasonable values compared to the observations mentioned in section 1.

Several other potentially important processes are excluded. Among them are pressure-dependent effects in seawater density, such as thermobaricity (Killworth 1977; Stewart and Haine 2016). The seawater thermodynamic calculations are at zero pressure in these experiments. This approximation is most suspect for the aW/SW entrainment parametrization as that process occurs at depth on the continental slope. Correcting for thermobaricity would increase the SW density relative to the aW density (because SW is colder and cold water is more compressible). That effect enhances entrainment for the reasons given above, although it is probably small as the entrainment does not occur at great depths. Cabbeling is also ignored, which is important for mixing at strong thermohaline fronts (Stewart et al. 2017) and potentially for upwelling of CDW in the Southern Ocean (Evans et al. 2018). Cabbeling creates anomalously dense water by mixing due to the curvature of isopycnals in thermohaline coordinates (see Fig. 3). The linear mixing formulae (like (13)–(15)) include it, but the impact on stratifying the water column is beyond the scope of this layer model. Interaction with ice sheets is also potentially important, especially in the Antarctic where glacial melt is significant (Jenkins et al. 2016; Abernathey et al. 2016; Dinniman et al.

2016). This source of freshwater depends on the ocean heat flux to the ice sheet, but the freshwater flux is specified here, regardless of the shelf circulation. Indeed, both the freshwater flux and the ocean heat loss flux $\mathcal{Q}$ are specified independently of the system state. They are also allowed to freely vary between shelf and basin, with only their sums constrained (supplement section S1). These assumptions are unrealistic because $\mathcal{Q}$, for instance, depends on sea ice cover. Refining these assumptions is beyond the present scope, partly because it requires more geometric parameters, like shelf area and depth: in the present model, the sea ice flux and sea ice thickness and concentration, which control $\mathcal{Q}$, are not linked.

Only steady solutions are shown, but in the real system time-dependent solutions may be important too, and they are intrinsically interesting. For time-dependence the model equations must be expanded to include water mass reservoir volumes, which will control the characteristic time scales for transient adjustment. One possibility is to couple the shelf and basin so they can exchange heat and salt anomalies. This coupling may resolve the degeneracy near the OW emergency into periodic solutions. Conceptually, it is easy to build an oscillator by adding negative feedback. Think of the OW temperature T_3 as a function of $\mathcal{N}^* \approx \mathcal{Q} + L\mathcal{F} - c_p \rho_1 T_1 U_1$ (from (29)). The OW temperature is high for low $\mathcal{Q}$ (or $\mathcal{N}^*$) from Fig. 6 (or 8), and vice versa, so the system output T_3 inverts the input signal $\mathcal{N}^*$. Allowing the OW temperature to control $\mathcal{N}^*$, by making U_1 depend on $T_1 - T_3$, for example, will trigger self-sustained oscillations. This mechanism has been proposed for low-frequency Atlantic Meridional Overturning Circulation variability because U_1 depends on $T_1 - T_3$ via the thermal wind relation (see Haine 2016 for a commentary and references therein).

5. Conclusions

This paper reports a conceptual model that specifies the strengths and thermohaline properties of polar estuarine and thermal overturning cells. The model satisfies mass, salt, and heat budgets

plus physical parametrizations for PW and OW formation. We explore the model characteristics and apply it to the Arctic and Antarctic termini of the global ocean overturning circulation. At best, the conceptual model is a caricature of a piece of the real system. It is most useful where it suggests characteristics of the estuarine and thermal overturning cells that are robust in more realistic models. Then it guides further research. The salient model characteristics are:

- The system is controlled by five flux parameters, namely the inflowing mass, heat, and freshwater fluxes, and the air/sea/ice heat and freshwater fluxes. However, the state is dominated by a single forcing parameter (eq. (29)) that is a linear combination of ocean heat loss flux, inflowing heat flux and ocean freshwater flux. This parameter measures the departure from a balanced volume budget between the estuarine and thermal overturning cells.

- A one-parameter infinity of solutions typically exists but the range of possible solutions can be tight. The solutions have different circulations onto and off the continental shelf, which links to overflow entrainment. This tradeoff permits switching between two states: the states exhibit strong (weak) shelf circulation, weak (strong) overflow entrainment, and large (small) heat flux from the ocean to the atmosphere. Switching allows the system to accommodate a wide range of inflow and air/sea/ice exchange fluxes and gives a bi-modal distribution of OW temperature with a narrow range of OW salinity.

- Solutions exist for limited flux parameters. Solutions disappear if the heat (salt) budget fails to balance because the system cannot export enough heat (salt). These heat (salt) crises collapse the estuarine cell. The thermal overturning cell is robust meaning that it can collapse in a so-called OW emergency, but it does not have to.

- For the Arctic, specifically the transfer across the Fram Strait and Barents Sea Opening, the real system appears vulnerable to heat crisis. The estuarine cell vanishes for increased

meteoric freshwater flux to the ocean, or increased AW heat flux, or decreased ocean heat loss flux. The first two factors are anticipated under global warming (Rawlins et al. 2010; Vavrus et al. 2012; Collins et al. 2013), pushing the Arctic closer to heat crisis and collapse of the estuarine cell. This may relate to Arctic Ocean "Atlantification" (Polyakov et al. 2017).

- For the Antarctic, the real system appears close to OW emergency with weak constraints on the strengths of the estuarine and thermal cells, although most solutions show a stronger estuarine cell. This result suggests that the Antarctic system is more susceptible to unforced variations than the Arctic. The sensitivity of the Antarctic solutions to changes in flux parameters is unclear because the system appears close to switching between strong and weak shelf circulation modes. Loss of parts of the estuarine cell may relate to loss of sea ice and PW in Weddell Sea polynyas (Comiso and Gordon 1987; Gordon 2014). Such offshore polynyas are linked to climate variations that are projected to strengthen with anthropogenic climate change (Campbell et al. 2019). Loss of the thermal cell may relate to loss of AABW formation in future climate projections (Lago and England 2019).

The most important lessons from this conceptual polar overturning model are probably these: The Arctic system is being driven towards heat crisis and collapse of the estuarine overturning cell by flux changes associated with anthropogenic climate change. Approaching the heat crisis, entrainment and shelf salinity are high, shelf circulation is weak, and variability in OW flux and temperature is small. Sea ice does not disappear prior to the heat crisis. The Antarctic system occupies a regime with large intrinsic variability between OW and PW fluxes and between strong and weak shelf circulations. The magnitude and sign of the sensitivity to changes in ocean heat loss, freshwater gain, and CDW heat flux are uncertain.

Data availability statement. The MATLAB software to compute solutions to the conceptual model in this paper is available at `https://github.com/ThomasHaine/polar_overturning_circulation_model`. An interactive app and the scripts to produce the figures are available.

Acknowledgments. This work was supported by grant 19-PO19-0025 from the National Aeronautics and Space Administration. Discussions with Ali Siddiqui, Miguel Jimenez-Urias, and Renske Gelderloos helped clarify the work and Bert Rudels inspired it.

References

Aagaard, K., L. K. Coachman, and E. Carmack, 1981: On the halocline of the Arctic Ocean. *Deep Sea Res., Part A*, **28 (6)**, 529–545, doi:10.1016/0198-0149(81)90115-1.

Aagaard, K., J. H. Swift, and E. C. Carmack, 1985: Thermohaline circulation in the Arctic Mediterranean Seas. *J. Geophys. Res.*, **90 (C3)**, 4833, doi:10.1029/jc090ic03p04833.

Abernathey, R. P., I. Cerovecki, P. R. Holland, E. Newsom, M. Mazloff, and L. D. Talley, 2016: Water-mass transformation by sea ice in the upper branch of the Southern Ocean overturning. *Nature Geoscience*, **9 (8)**, 596–601, doi:10.1038/ngeo2749.

Boyer, T. P., and Coauthors, 2018: World ocean database 2018. Tech. rep., NOAA Atlas NESDIS 87. Https://data.nodc.noaa.gov/woa/WOD/DOC/wod_intro.pdf.

Campbell, E. C., E. A. Wilson, G. W. K. Moore, S. C. Riser, C. E. Brayton, M. R. Mazloff, and L. D. Talley, 2019: Antarctic offshore polynyas linked to Southern Hemisphere climate anomalies. *Nature*, **570 (7761)**, 319–325, doi:10.1038/s41586-019-1294-0.

Cenedese, C., and C. Adduce, 2010: A new parameterization for entrainment in overflows. *J. Phys. Oceanogr.*, **40 (8)**, 1835–1850, doi:10.1175/2010jpo4374.1.

612 Collins, M., and Coauthors, 2013: Long-term climate change: Projections, commitments and
613 irreversibility. *Climate Change 2013: The Physical Science Basis. Contribution of Working*
614 *Group I to the Fifth Assessment Report of the Intergovernmental Panel on Climate Change*, T. F.
615 Stocker, D. Qin, G.-K. Plattner, M. Tignor, S. K. Allen, J. Boschung, A. Nauels, Y. Xia, V. Bex,
616 and P. M. Midgley, Eds., Cambridge University Press, Cambridge, United Kingdom and New
617 York, NY, USA.

618 Comiso, J. C., and A. L. Gordon, 1987: Recurring polynyas over the Cosmonaut Sea and the Maud
619 Rise. *J. Geophys. Res.*, **92 (C3)**, 2819, doi:10.1029/jc092ic03p02819.

620 Dinniman, M., X. Asay-Davis, B. Galton-Fenzi, P. Holland, A. Jenkins, and R. Timmermann,
621 2016: Modeling ice shelf/ocean interaction in Antarctica: A review. *Oceanography*, **29 (4)**,
622 144–153, doi:10.5670/oceanog.2016.106.

623 Eldevik, T., and J. E. Ø. Nilsen, 2013: The Arctic–Atlantic thermohaline circulation. *J. Climate*,
624 **26 (21)**, 8698–8705, doi:10.1175/jcli-d-13-00305.1.

625 Ellison, T. H., and J. S. Turner, 1959: Turbulent entrainment in stratified flows. *J. Fluid Mech.*,
626 **6 (03)**, 423, doi:10.1017/s0022112059000738.

627 Evans, D. G., J. D. Zika, A. C. Naveira Garabato, and A. J. G. Nurser, 2018: The cold
628 transit of Southern Ocean upwelling. *Geophys. Res. Lett.*, **45 (24)**, 13,386–13,395, doi:
629 10.1029/2018gl079986.

630 Foster, T. D., and E. C. Carmack, 1976: Frontal zone mixing and Antarctic bottom water formation
631 in the southern Weddell Sea. *Deep Sea Res.*, **23**, 301–317.

632 Gill, A. E., 1973: Circulation and bottom water production in the Weddell Sea. *Deep Sea Res.*, **20**,
633 111–140, doi:10.1016/0011-7471(73)90048-x.

Gordon, A. L., 2014: Southern Ocean polynya. *Nature Climate Change*, **4 (4)**, 249–250, doi: 10.1038/nclimate2179.

Haine, T. W. N., 2016: Ocean science: Vagaries of Atlantic overturning. *Nature Geoscience*, **9**, 479–480, doi:10.1038/ngeo2748.

Haine, T. W. N., and Coauthors, 2015: Arctic freshwater export: Status, mechanisms, and prospects. *Glob. Planet. Change*, **125**, 13–35, doi:10.1016/j.gloplacha.2014.11.013.

Hansen, B., and S. Østerhus, 2000: North Atlantic-Nordic Seas exchange. *Prog. Oceanogr.*, **45**, 109–208.

Hansen, B., S. Østerhus, W. R. Turrell, S. Jónsson, H. Valdimarsson, H. Hátún, and S. M. Olsen, 2008: The inflow of Atlantic water, heat, and salt to the Nordic Seas across the Greenland-Scotland ridge. *Arctic-Subarctic Ocean Fluxes: Defining the role of the Northern Seas in Climate*, R. R. Dickson, J. Meincke, and P. Rhines, Eds., Springer-Verlag, 15–43, doi:10.1007/978-1-4020-6774-7_2.

Jacobs, S. S., 2004: Bottom water production and its links with the thermohaline circulation. *Antarctic Science*, **16 (4)**, 427–437, doi:10.1017/s095410200400224x.

Jenkins, A., P. Dutrieux, S. Jacobs, E. Steig, H. Gudmundsson, J. Smith, and K. Heywood, 2016: Decadal ocean forcing and Antarctic ice sheet response: Lessons from the Amundsen Sea. *Oceanography*, **29 (4)**, 106–117, doi:10.5670/oceanog.2016.103.

Killworth, P. D., 1977: Mixing on the Weddell Sea continental slope. *Deep Sea Res.*, **24**, 427–448.

Klinger, B. A., and T. W. N. Haine, 2019: *Ocean Circulation in Three Dimensions*. 1st ed., Cambridge University Press, Cambridge, United Kingdom and New York, NY, USA, URL http://www.cambridge.org/9780521768436.

Lago, V., and M. H. England, 2019: Projected slowdown of Antarctic bottom water formation in response to amplified meltwater contributions. *J. Climate*, **32 (19)**, 6319–6335, doi:10.1175/jcli-d-18-0622.1.

Lambert, E., T. Eldevik, and M. A. Spall, 2018: On the dynamics and water mass transformation of a boundary current connecting alpha and beta oceans. *J. Phys. Oceanogr.*, **48 (10)**, 2457–2475, doi:10.1175/jpo-d-17-0186.1.

Marshall, J., and K. Speer, 2012: Closure of the meridional overturning circulation through Southern Ocean upwelling. *Nature Geoscience*, **5**, 171–180, doi:10.1038/ngeo1391.

Maus, S., 2003: Interannual variability of dense shelf water salinities in the north-western Barents Sea. *Polar Research*, **22 (1)**, 59–66, doi:10.3402/polar.v22i1.6444.

Muench, R., L. Padman, A. Gordon, and A. Orsi, 2009: A dense water outflow from the Ross Sea, Antarctica: Mixing and the contribution of tides. *J. Mar. Res.*, **77 (4)**, 369–387, doi:10.1016/j.jmarsys.2008.11.003.

Naveira Garabato, A. C., E. L. McDonagh, D. P. Stevens, K. J. Heywood, and R. J. Sanders, 2002: On the export of Antarctic Bottom Water from the Weddell Sea. *Deep Sea Res., Part II*, **49 (21)**, 4715–4742, doi:10.1016/s0967-0645(02)00156-x.

Orsi, A. H., G. C. Johnson, and J. L. Bullister, 1999: Circulation, mixing, and production of Antarctic bottom water. *Prog. Oceanogr.*, **43**, 55–109, doi:10.1016/s0079-6611(99)00004-x.

Østerhus, S., W. R. Turrell, S. Jónsson, and B. Hansen, 2005: Measured volume, heat, and salt fluxes from the Atlantic to the Arctic Mediterranean. *Geophys. Res. Lett.*, **32**, doi:10.1029/2004GL022188.

Ottolenghi, L., C. Cenedese, and C. Adduce, 2017: Entrainment in a dense current flowing down a rough sloping bottom in a rotating fluid. *J. Phys. Oceanogr.*, **47 (3)**, 485–498, doi: 10.1175/jpo-d-16-0175.1.

Padman, L., S. L. Howard, A. H. Orsi, and R. D. Muench, 2009: Tides of the northwestern Ross Sea and their impact on dense outflows of Antarctic Bottom Water. *Deep Sea Res., Part II*, **56 (13-14)**, 818–834, doi:10.1016/j.dsr2.2008.10.026.

Pellichero, V., J.-B. Sallée, C. C. Chapman, and S. M. Downes, 2018: The southern ocean meridional overturning in the sea-ice sector is driven by freshwater fluxes. *Nature Communications*, **9 (1)**, doi:10.1038/s41467-018-04101-2.

Polyakov, I. V., and Coauthors, 2017: Greater role for Atlantic inflows on sea-ice loss in the Eurasian Basin of the Arctic Ocean. *Science*, **356 (6335)**, 285–291, doi:10.1126/science.aai8204.

Price, J. F., and M. O'Neil Baringer, 1994: Outflows and deep water production by marginal seas. *Prog. Oceanogr.*, **33**, 161–200, doi:10.1016/0079-6611(94)90027-2.

Quadfasel, D., B. Rudels, and K. Kurz, 1988: Outflow of dense water from a Svalbard fjord into the Fram Strait. *Deep Sea Res., Part A*, **35 (7)**, 1143–1150, doi:10.1016/0198-0149(88)90006-4.

Rawlins, M. A., and Coauthors, 2010: Analysis of the Arctic system for freshwater cycle intensification: Observations and expectations. *J. Climate*, **21**, 5715–5737, doi:10.1175/2010JCLI3421.1.

Rudels, B., 2010: Constraints on exchanges in the Arctic Mediterranean—do they exist and can they be of use? *Tellus*, **62A**, 109–122, doi:10.1111/j.1600-0870.2009.00425.x.

Rudels, B., 2012: Arctic Ocean circulation and variability - advection and external forcing encounter constraints and local processes. *Ocean Sci.*, **8**, 261–286, doi:10.5194/os-8-261-2012.

Rudels, B., 2016: Arctic Ocean stability: The effects of local cooling, oceanic heat transport, freshwater input, and sea ice melt with special emphasis on the Nansen basin. *J. Geophys. Res.*, **121**, doi:10.1002/2015JC011045.

Rudels, B., E. Fahrbach, J. Meincke, G. Budéus, and P. Eriksson, 2002: The East Greenland Current and its contribution to the Denmark Strait overflow. *ICES J. Mar. Sci.*, **59**, 1133–1154, doi:10.1006/jmsc.2002.1284.

Rudels, B., and D. Quadfasel, 1991: Convection and deep water formation in the Arctic Ocean-Greenland Sea system. *J. Mar. Sys.*, **2 (3-4)**, 435–450, doi:10.1016/0924-7963(91)90045-v.

Stewart, A. L., A. Klocker, and D. Menemenlis, 2018: Circum-Antarctic shoreward heat transport derived from an eddy- and tide-resolving simulation. *Geophys. Res. Lett.*, **45 (2)**, 834–845, doi:10.1002/2017gl075677.

Stewart, K. D., and T. W. N. Haine, 2016: Thermobaricity in the transition zones between alpha and beta oceans. *J. Phys. Oceanogr.*, **46 (6)**, 1805–1821, doi:10.1175/jpo-d-16-0017.1.

Stewart, K. D., T. W. N. Haine, A. M. Hogg, and F. Roquet, 2017: On cabbeling and thermobaricity in the surface mixed layer. *J. Phys. Oceanogr.*, **47**, 1775–1787, doi:10.1175/jpo-d-17-0025.1.

Talley, L., 2013: Closure of the global overturning circulation through the Indian, Pacific, and Southern Oceans: Schematics and transports. *Oceanography*, **26 (1)**, 80–97, doi:10.5670/oceanog.2013.07.

Tamura, T., and K. I. Ohshima, 2011: Mapping of sea ice production in the Arctic coastal polynyas. *J. Geophys. Res.*, **116 (C7)**, doi:10.1029/2010jc006586.

Tsubouchi, T., and Coauthors, 2012: The Arctic Ocean in summer: A quasi-synoptic inverse estimate of boundary fluxes and water mass transformation. *J. Geophys. Res.*, **117**, C01 024, doi:10.1029/2011JC007174.

Tsubouchi, T., and Coauthors, 2018: The Arctic Ocean seasonal cycles of heat and freshwater fluxes: observation-based inverse estimates. *J. Phys. Oceanogr.*, doi:10.1175/jpo-d-17-0239.1.

Turner, J. S., 1986: Turbulent entrainment: the development of the entrainment assumption, and its application to geophysical flows. *J. Fluid Mech.*, **173**, 431–471, doi:10.1017/s0022112086001222.

Vavrus, S. J., M. M. Holland, A. Jahn, D. Bailey, and B. A. Blazey, 2012: Twenty-first-century Arctic climate change in CCSM4. *J. Climate*, **25**, 2696–2710, doi:10.1175/JCLI-D-11-00220.1.

Volkov, D. L., L.-L. Fu, and T. Lee, 2010: Mechanisms of the meridional heat transport in the Southern Ocean. *Ocean. Dyn.*, **60 (4)**, 791–801, doi:10.1007/s10236-010-0288-0.

LIST OF TABLES

TABLE 1. Table of notation. AW = Atlantic Water (subscript 1), PW = Polar Water (subscript 2), OW = Overflow Water (subscript 3), aW = ambient Water. See also Fig. 2.

Symbol	Unit	Meaning
Parameters		
U_1, T_1, S_1	Sv, °C, g/kg	AW volume flux, temperature, salinity at gateway
$Q = Q_b + Q_s$	W	Ocean heat flux (total = basin + shelf)
$\mathcal{F} = \mathcal{F}_b + \mathcal{F}_s$	kgs^{-1}	Ocean freshwater flux (total = basin + shelf)
ϕ	(no unit)	Fraction of PW to AW entrained into OW
$\mathcal{N}^*$	W	Compound forcing parameter from (29)
Variables		
U_2, U_3, U_i	Sv	PW, OW, sea ice volume flux at gateway
u_1, u_i	Sv	AW, sea ice volume flux at shelf break
S_s	g/kg	SW salinity
Intermediate variables		
S_2	g/kg	PW salinity
T_3, S_3	°C, g/kg	OW temperature, salinity
T_a, S_a	°C, g/kg	aW temperature, salinity
u_s	Sv	SW volume flux at shelf break
$\rho_1, \rho_2, \rho_3, \rho_a$	kgm^{-3}	AW, PW, OW, aW density
Φ	(no unit)	Entrainment fraction
Constants		
T_i, S_i	°C, g/kg	Sea ice temperature, salinity
$T_2 = T_s = T_f$	°C	PW, SW, freezing temperature
ρ_i, ρ_0	kgm^{-3}	Sea ice, characteristic seawater density
c_p, c_i	$\mathrm{Jkg}^{-1}\mathrm{K}^{-1}$	Seawater, sea ice specific heat capacity
L	Jkg^{-1}	Latent heat of fusion
α, β	$^{\circ}\mathrm{C}^{-1}$, kg/g	Thermal expansion, haline contraction coefficients
γ	$\mathrm{kg}^{2/3}\mathrm{s}^{1/3}\mathrm{m}^{-3}$	Entrainment parameter in (17)

738 TABLE 2. Table of Experiments. The mixing fraction $\phi = 0.33$; see section 3h for a discussion. For all
739 experiments $\delta\Phi = 0.01$ (see supplement section S1).

Experiment	Description	U_1	T_1	S_1	Q	$-\mathcal{F}$
		Sv	^{o}C	g/kg	TW	$\times 10^9 \mathrm{kgs}^{-1}$
1	Fram Strait+BSO	4.75	3.40	35.00	115	180
2	Fram Strait+BSO high Q	4.75	3.40	35.00	153	180
3	Fram Strait+BSO various Q	4.75	3.40	35.00	87–195	180
4	Fram Strait+BSO various parameters	3.17–7.13	2.55–4.53	34.30–35.70	70–280	75–300
5	Fram Strait+BSO various S_2	4.75	3.40	35.00	115	180
6	Antarctic	26.0	0.50	34.67	300	240

LIST OF FIGURES

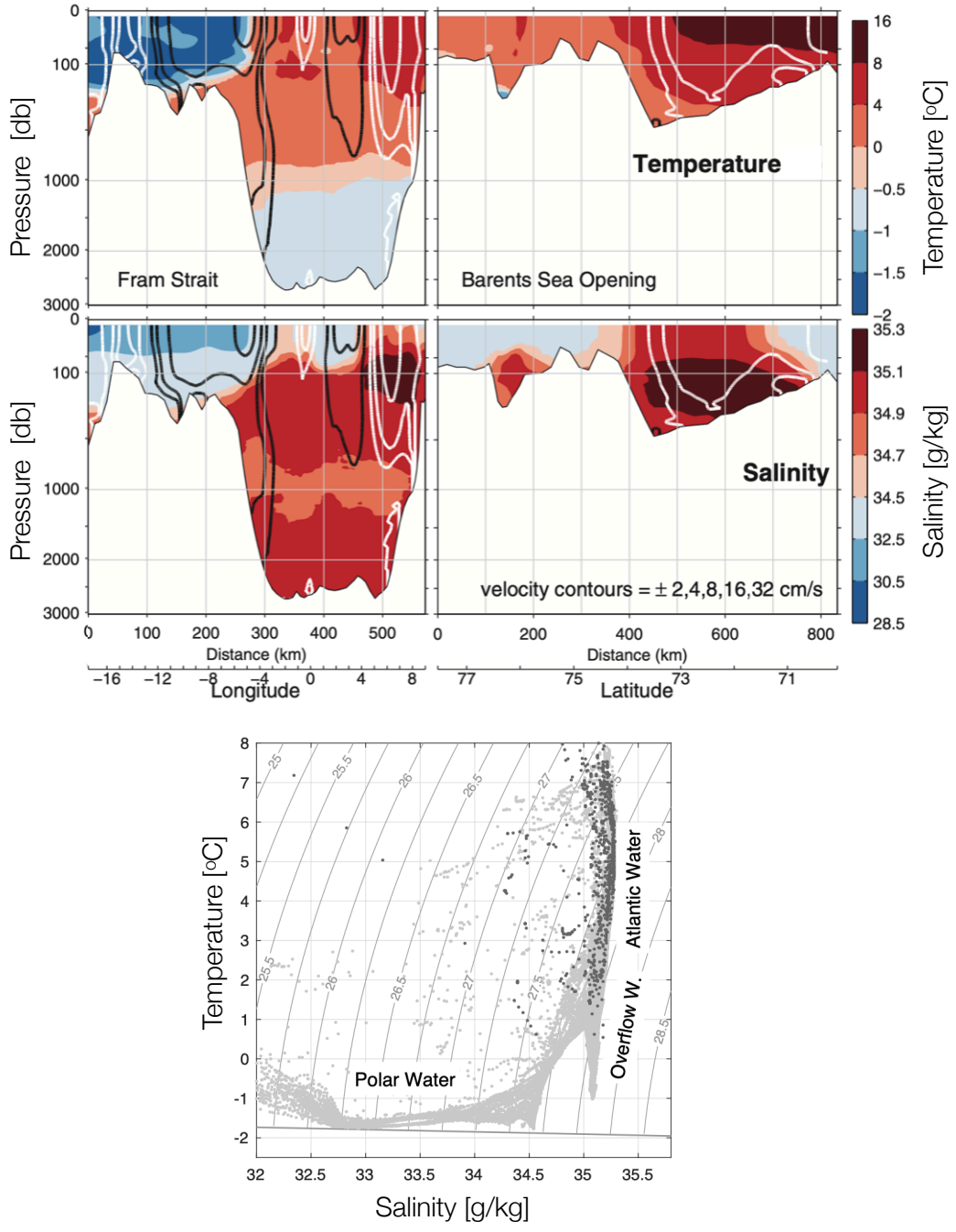

FIG. 1. Upper two panels: Observations of temperature, salinity and normal geostrophic current across the Fram Strait and Barents Sea Opening. Modified from Klinger and Haine (2019) and based on results from Tsubouchi et al. (2012). Lower panel: Temperature and salinity data from Fram Strait in August 2002 (light gray) and from the Barents Sea Opening in August 2017 (dark gray; from the World Ocean Database, Boyer et al. 2018).

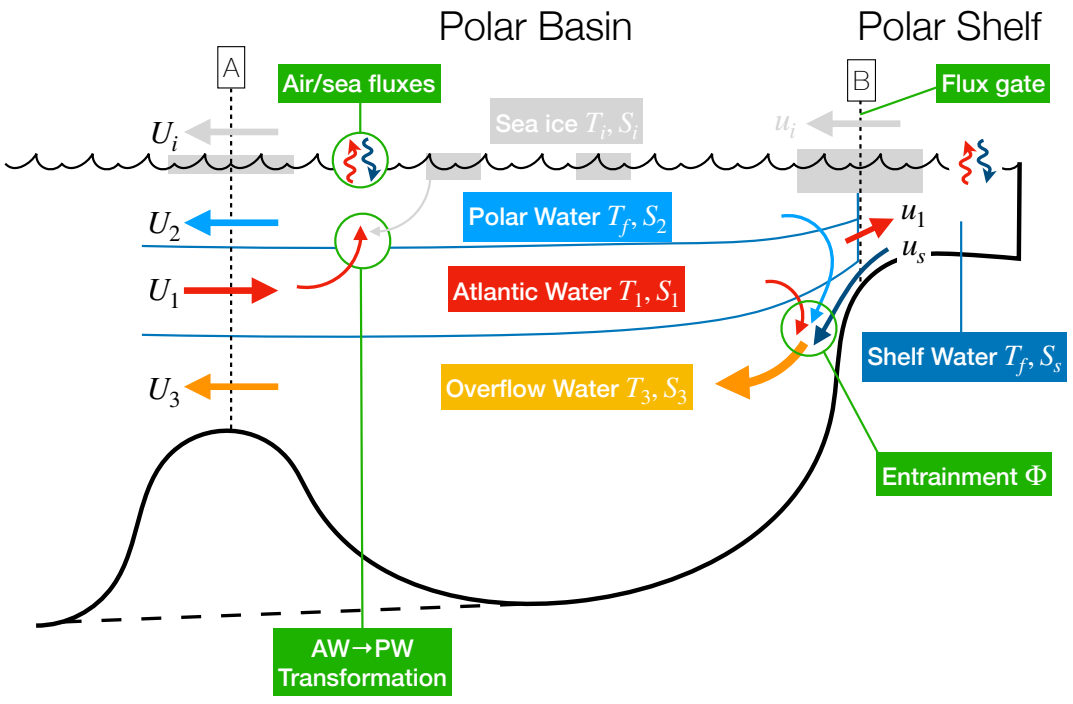

806 FIG. 2. Schematic of the conceptual polar overturning model. The sign convention is that positive volume
807 fluxes are towards the right. For plausible solutions $\{U_2, U_3, U_i, u_s, u_i\} < 0$ and $u_1 > 0$, as the arrows show. The
808 bathymetric bump at section A (nominally, the Fram Strait and Barents Sea Opening) is for illustrative purposes:
809 the dashed line represents the Antarctic case. Table 1 defines the symbols.

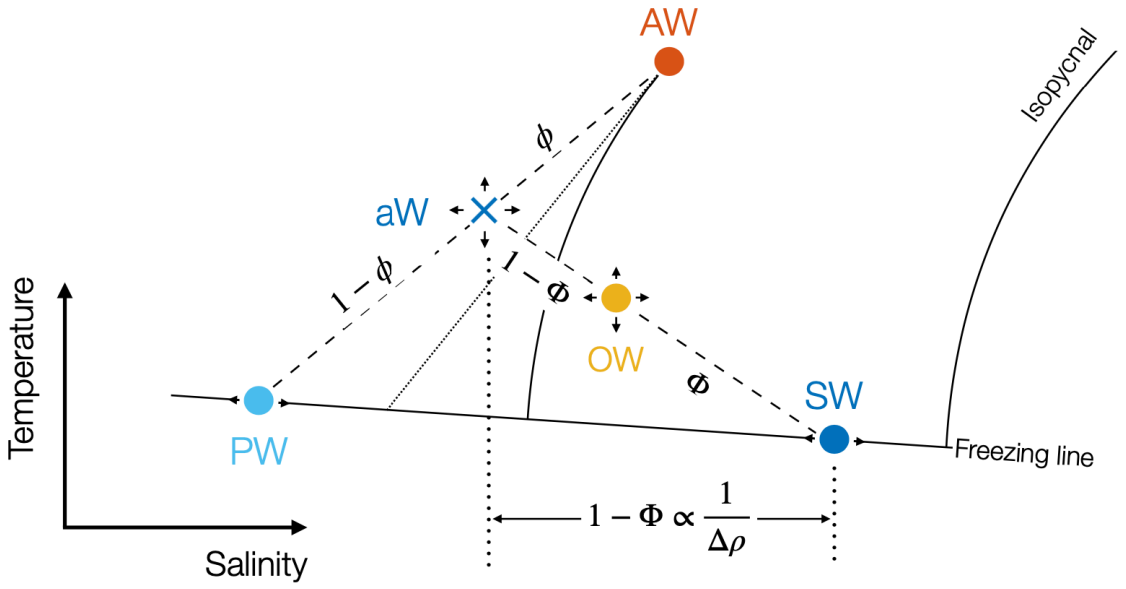

FIG. 3. Schematic of the processes affecting OW properties. The Atlantic Water (AW) properties are specified. The Polar Water (PW) properties are freezing temperature and salinity less than the maximum value given by the dotted line tangent to the AW isopycnal. The ambient Water (aW) properties are a mixture of PW and AW determined by ϕ. The Overflow Water (OW) properties are a mixture of aW and SW determined by entrainment Φ. The entrainment Φ depends on the density difference $\Delta\rho$ between aW and SW from (17).

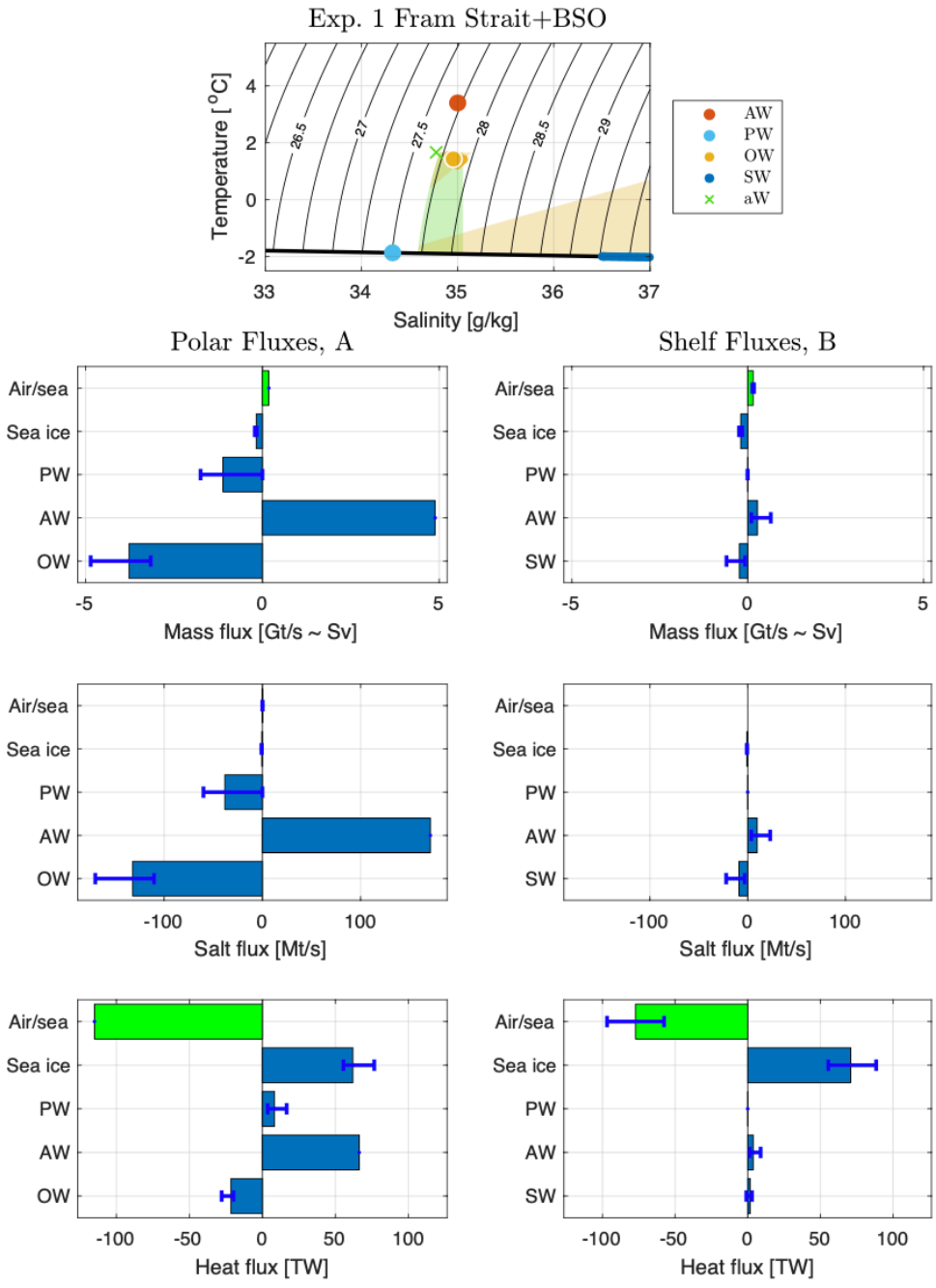

FIG. 4. Results for experiment 1, with parameters appropriate for the Arctic (Fram Strait and Barents Sea Opening, BSO). The upper panel shows temperature/salinity properties T_i, S_i for AW ($i = 1$), SW ($i = s$), aW ($i = a$), OW ($i = 3$), and PW ($i = 2$). The curved black contours are the density anomaly $\rho(T, S) - 1000\text{kgm}^{-3}$. The thick black line is the freezing temperature. The brown and green patches show the range of possible OW properties from the theories in supplement sections S5 and S6, respectively. The left (right) column of panels show mass, salt, and heat fluxes crossing section A (B) in Fig. 2. The individual terms in (S1) and (S2) are shown with the horizontal bars. The blue error bars indicate the range of possible solutions (see text). This solution is entrainment dominated with $\Phi \approx 0.94$, warm OW, and a weak shelf circulation.

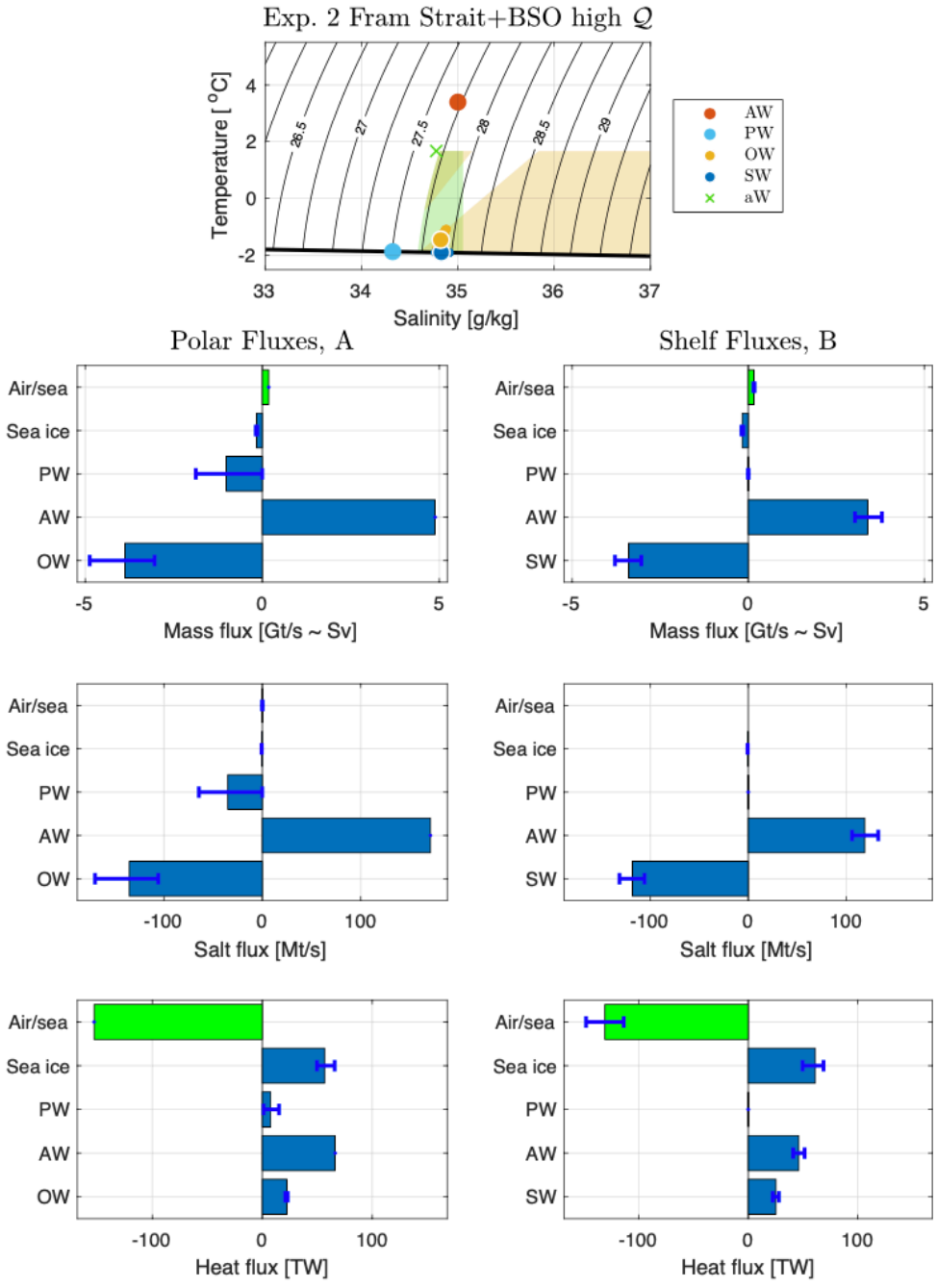

823 FIG. 5. As Fig. 4, except for experiment 2. This solution has similar mass and salt fluxes to experiment 1
824 shown in Fig. 4, but weak entrainment ($\Phi \approx 0.13$), strong shelf circulation, and cold OW. The total ocean heat
825 loss flux, Q is 33% times larger than for experiment 1. Notice the heat flux abscissa limits differ from Fig. 4.

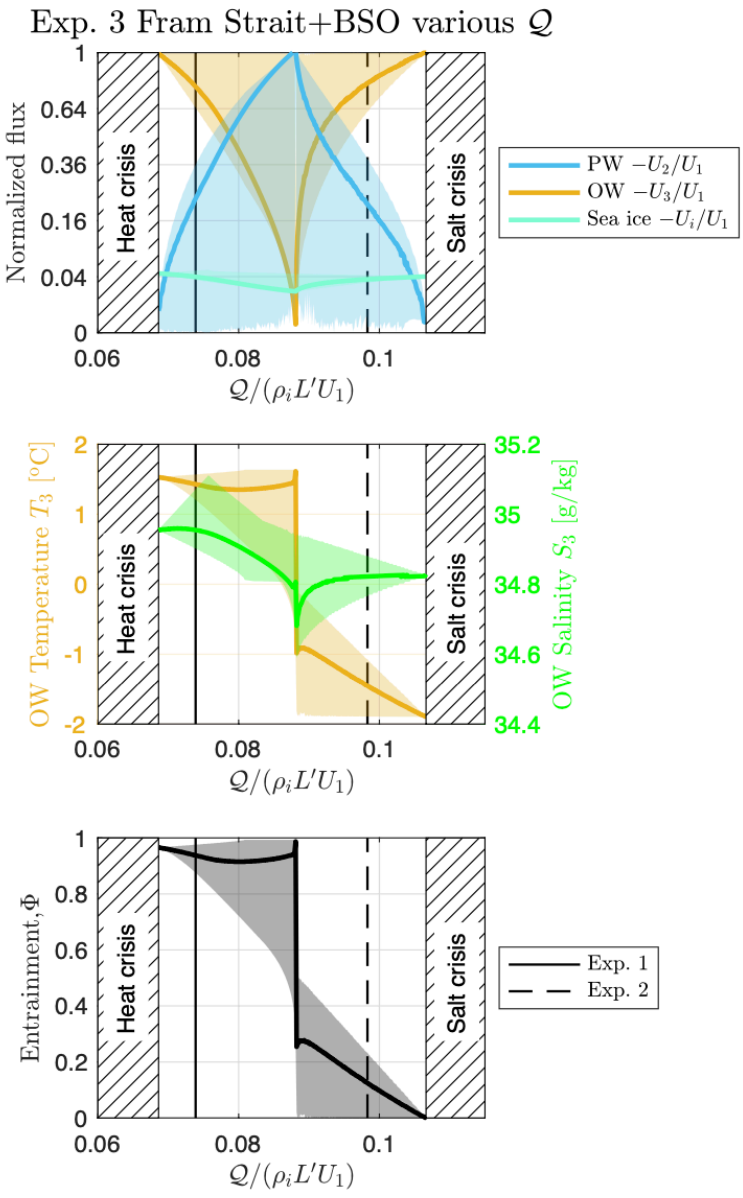

826 FIG. 6. Results for experiment 3 for the Arctic. The top panel shows the normalized volume fluxes U_2, U_3,
827 and U_i. The middle panel shows the OW properties T_3 and S_3. The bottom panel shows the entrainment Φ. In
828 each case, the abscissa is the normalized ocean heat loss flux $\mathcal{Q}$. The solid and dashed vertical lines indicate
829 experiments 1 and 2, shown in Figs. 4 and 5, respectively. The hatched regions indicate no solutions are possible
830 because $U_2 \not< 0$; see text for details.

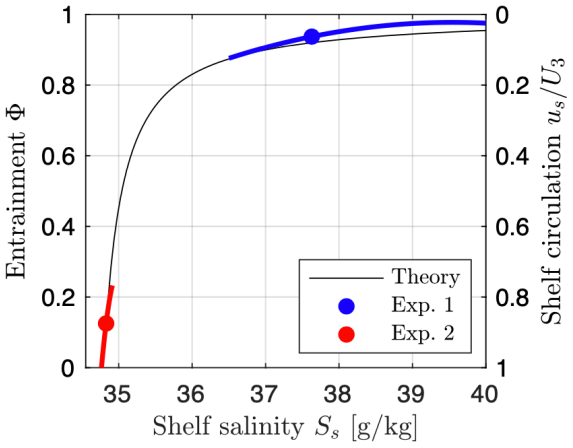

FIG. 7. Schematic of the tradeoff between entrainment Φ and shelf salinity S_s for fixed OW flux. Strong (weak) entrainment implies weak (strong) shelf circulation u_s from (21). Results from experiments 1 and 2, including the range of possible solutions, are shown. The theory curve is from (28).

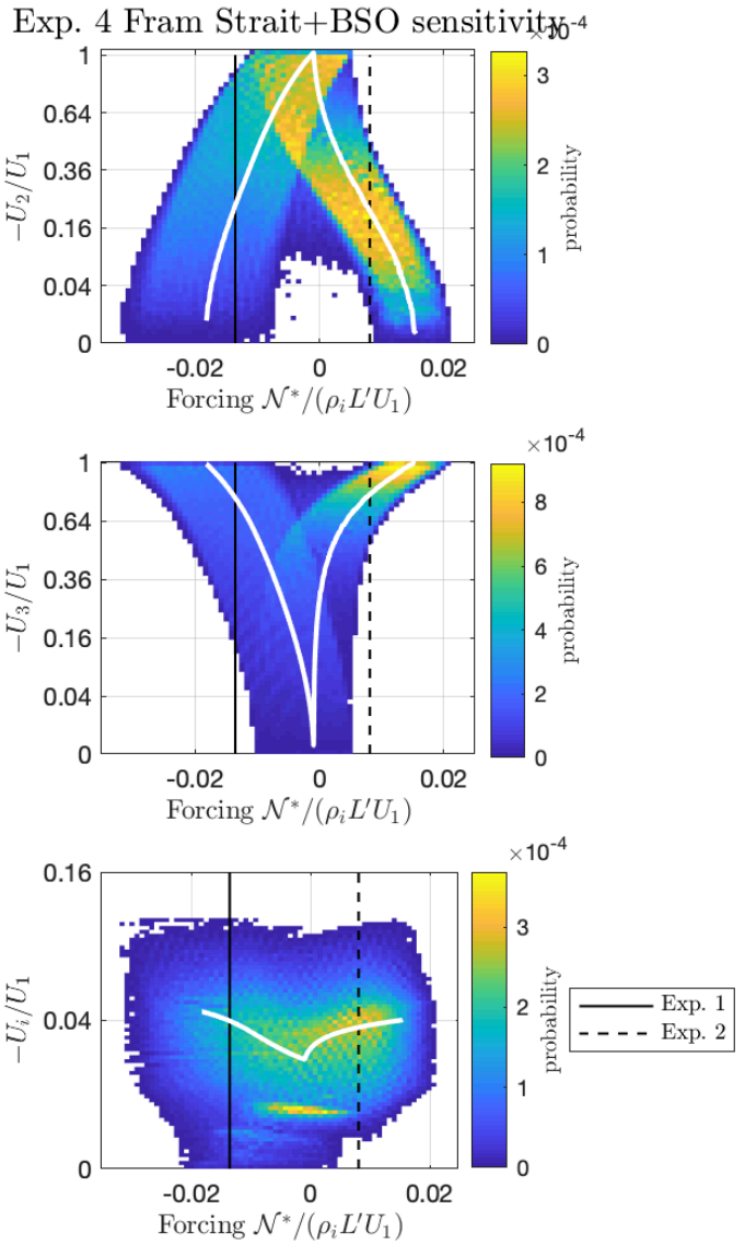

834 FIG. 8. Results for experiment 4 for the Arctic. Normalized distributions of U_2, U_3, and U_i against the
835 forcing parameter $\mathcal{N}^* = L'\mathcal{F} + (1 - S_i/S_1)\,\mathcal{Q} + c_p\rho_0\,(S_i/S_1 - 1)\,T_1 U_1$ for many solutions with different parameters
836 $\{\mathcal{F}, \mathcal{Q}, U_1, T_1, S_1\}$ (see Table 2). In each case, the distribution is taken of the solutions with entrainment closest to
837 the mean entrainment, like the bars in Fig. 4. The solid and dashed vertical lines indicate experiments 1 and 2,
838 shown in Figs. 4 and 5, respectively. The white curves show the results from experiment 3, as in Fig. 6, which
839 are a subset of the results from experiment 4. There are 525199 valid solutions in experiment 4.

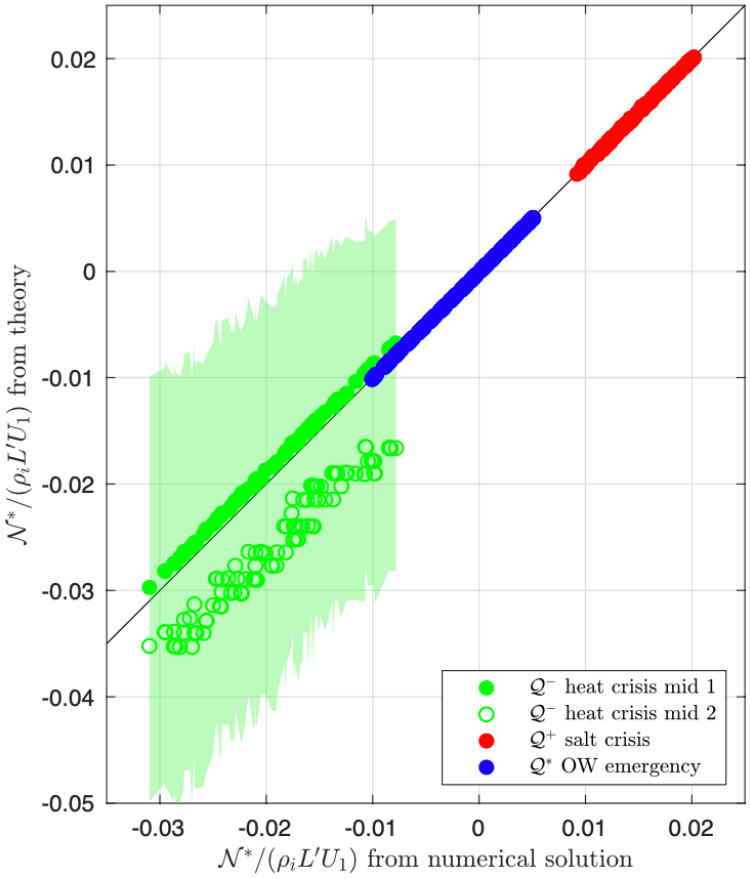

FIG. 9. Parametric locations of heat and salt crises, and OW emergency. The abscissa plots normalized forcing parameter $\mathcal{N}^* = L'\mathcal{F} + (1 - S_i/S_1)\,\mathcal{Q} + c_p \rho_0 \,(S_i/S_1 - 1)\,T_1 U_1$ from the numerical solutions to experiments 4. The ordinate plots the corresponding values of $\mathcal{N}^*$ from the theory in supplement section S4. The black diagonal line indicates perfect agreement between theory and the numerical results.

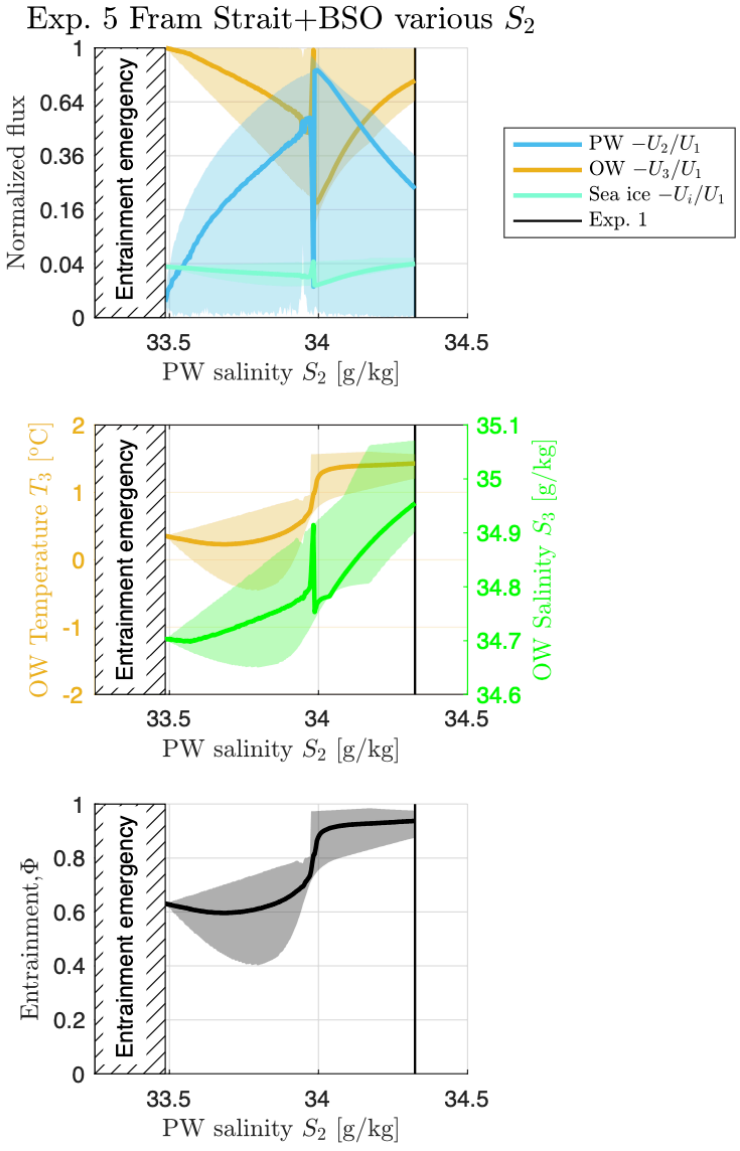

FIG. 10. As Fig. 6, except for experiment 5, illustrating the approach to the entrainment emergency.

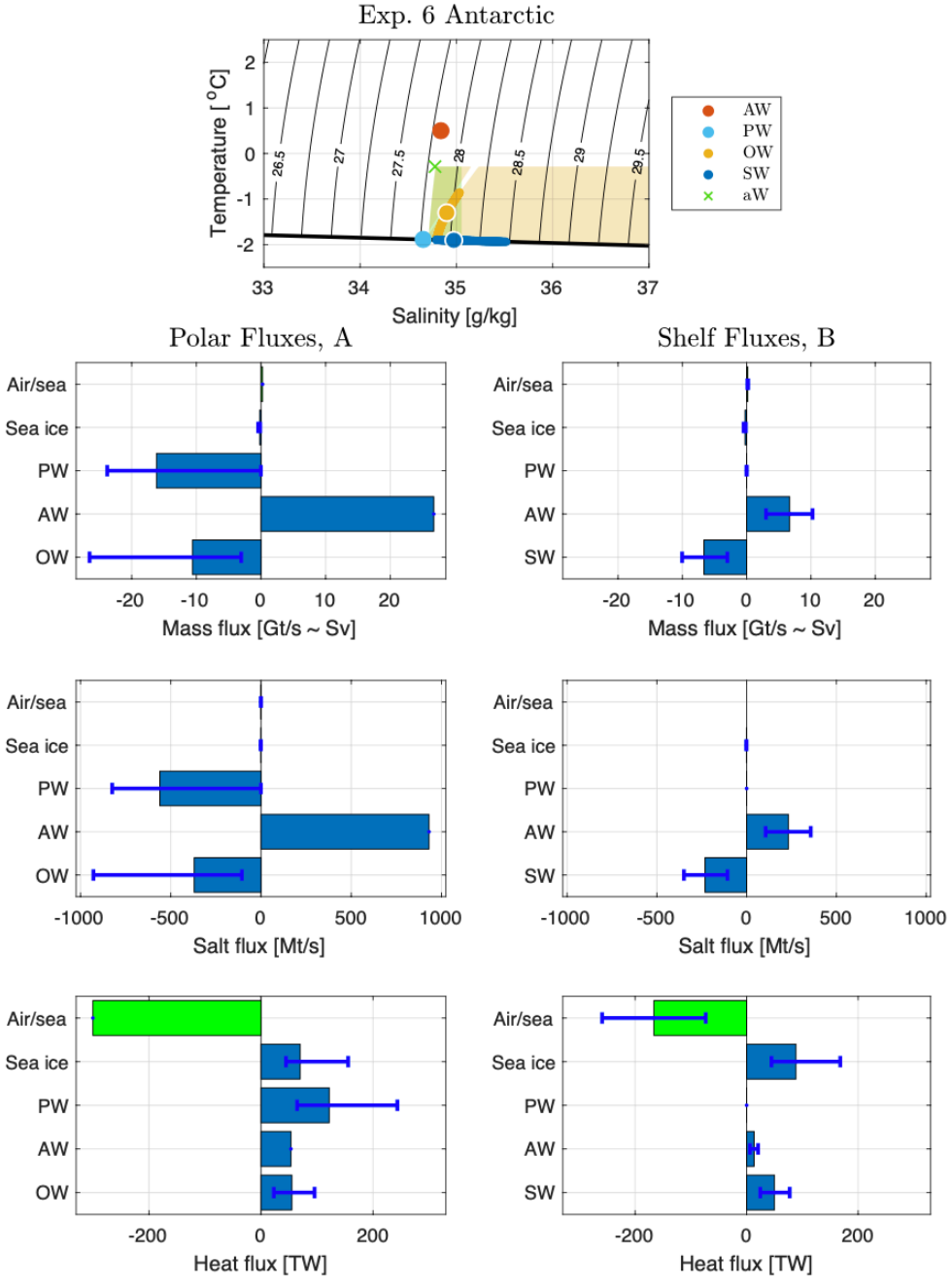

FIG. 11. As Fig. 4, except for experiment 6 for the Antarctic.

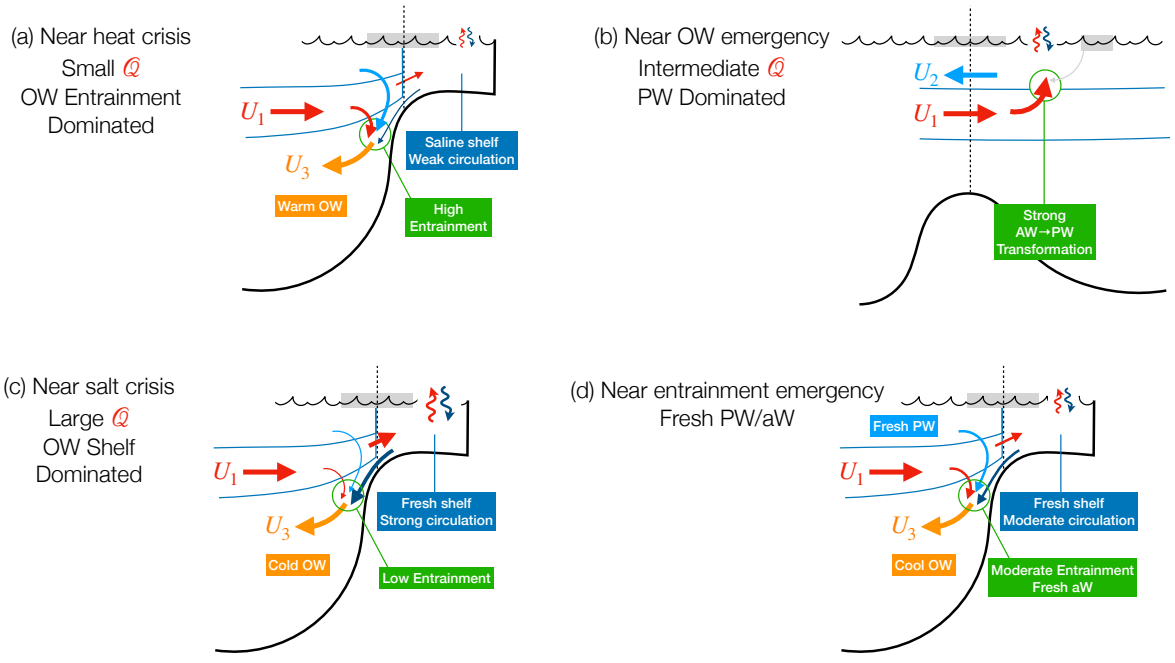

FIG. 12. Schematics of the four main solution modes: (a) Heat crisis for small Q (like experiment 1), (b) OW emergency for intermediate Q (like experiment 6 and the middle of experiment 3), (c) Salt crisis for large Q (like experiment 2), and (d) Entrainment emergency for fresh PW and/or aW (like the small PW salinity end of experiment 5). These main solutions are determined by the forcing, indicated by the ocean heat loss flux Q (Figs. 6 and 8), and by the aW salinity (Fig. 10). See also supplement Fig. S1.